An energy conservative method to predict the erosive aggressiveness of collapsing cavitating structures and cavitating flows from numerical simulations

Schenke, Sören; van Terwisga, Tom J.C.

DOI
10.1016/j.ijmultiphaseflow.2018.11.016

Publication date
2019

Document Version
Final published version

Published in
International Journal of Multiphase Flow

International Journal of Multiphase Flow 111 (2019) 200–218

Contents lists available at ScienceDirect

International Journal of Multiphase Flow

journal homepage: www.elsevier.com/locate/ijmulflow

An energy conservative method to predict the erosive aggressiveness of collapsing cavitating structures and cavitating flows from numerical simulations

Sören Schenke[a,*], Tom J.C. van Terwisga[a,b]

[a] Delft University of Technology, Netherlands
[b] Maritime Research Institute Netherlands, Netherlands

ARTICLE INFO

Article history:
Received 25 June 2018
Revised 27 November 2018
Accepted 27 November 2018
Available online 30 November 2018

Keywords:
Cavitation erosion
Impact power
Multiphase flow simulation

ABSTRACT

A new technique is proposed in this study to assess the erosive aggressiveness of cavitating flows from numerical flow simulations. The technique is based on the cavitation intensity approach by Leclercq et al. (2017), predicting the instantaneous surface impact power of collapsing cavities from the potential energy hypothesis (see Hammitt, 1963; Vogel and Lauterborn, 1988). The cavitation intensity approach by Leclercq et al. (2017) is further developed and the amount of accumulated surface energy caused by the near wall collapse of idealized cavity types is verified against analytical predictions. Furthermore, two different impact power functions are introduced to compute a weighted time average of the impact power distribution caused by the cavity collapses in cavitating flows. The extreme events are emphasized to an extent specified by a single model parameter. Thus, the impact power functions provide a physical measure of the cavitating flow aggressiveness. This approach is applied to four idealized cavities, as well as to the cavitating flow around a NACA0015 hydrofoil. Areas subjected to aggressive cavity collapse events are identified and the results are compared against experimental paint test results by Van Rijsbergen et al. (2012) and the numerical erosion risk assessment by Li et al. (2014). The model is implemented as a runtime post-processing tool in the open source CFD environment OpenFOAM (2018), employing the inviscid Euler equations and mass transfer source terms to model the cavitating flow.

1. Introduction

Cavitation erosion is a problem in a wide range of fluid machinery involving liquid flows. Ship propellers, rudders, hydro pumps and turbines or diesel injectors are some of the most common examples. Cavitation occurs at locations of high local flow velocity, where pressure may drop as low as for the liquid phase to vaporize. The violent collapse of cavitating structures in regions of pressure recovery can result in high pressure loads and severe damage of such devices. Consequently, there is a need for numerical tools that can predict the risk of cavitation erosion at an early design stage. Cavitation erosion models are typically implemented as runtime post-processing tools in numerical flow solvers. For this reason, the capabilities and accuracy provided by the cavitating flow solver should be taken into account in the design of these models. When it comes to engineering applications, pressure based methods are still predominantly used to simulate cavitating flows. This is partially due to their robustness and rather low computational cost, but also because they can solve for (almost) incompressible flow regimes in a straight forward fashion. If the pure liquid and vapor phase of the flow can be considered as incompressible, mass transfer source terms are widely used to model cavitation. Compressibility is then only mimicked in regions subjected to phase transition. An overview of commonly used mass transfer models is found in the work by Frikha et al. (2009) and in the work by Morgut and Nobile (2011). It has been shown that these models are at least able to correctly reflect the inertia driven kinematics of cavitating flows. Model parameter independent results for the cavity collapse time (see Bhatt et al., 2015; Schenke and van Terwisga, 2017; Ghahramani and Bensow, 2018) and the frequency of cyclic cavitation (Schenke and van Terwigsa, 2017) are obtained in the limit of large model coefficients in combination with sufficient temporal resolution. In this limit, the mass transfer source terms always provide enough capacity to establish the equilibrium flow condition as defined by Sezal (2009), where the time scale of phase transition is not important within the advective time scale of the flow. The

* Corresponding author.
E-mail address: s.schenke@tudelft.nl (S. Schenke).

https://doi.org/10.1016/j.ijmultiphaseflow.2018.11.016
0301-9322/

density-pressure trajectory then remains close to vapor pressure during phase transition and the behavior of more realistic thermodynamic models is mimicked (see Koukouvinis and Gavaises, 2015; Schenke and van Terwigsa, 2017). The amplitudes of collapse pressure loads, however, have been shown to strongly depend on numerical settings for mass transfer model constants and time step size (see Schenke and van Terwisga, 2017; Ghahramani and Bensow, 2018). In this case, the risk of cavitation erosion should preferably be assessed from kinematic features of the collapsing cavities. The relevance of kinematic features of collapsing cavities for the flow aggressiveness has been hypothesized by Bark et al. (2004).

The design of cavition erosion models is further driven by the question what the most essential mechanism of cavitation erosion would be. An ongoing debate concerns the question whether cavitation erosion is predominantly caused by liquid micro-jets or by collapse induced shock waves impacting the solid surface. It is not straight forward to entirely separate both effects from each other, because the liquid jet induced impact pressure is for one part formed by a water hammer at the moment of jet incidence. The water hammer pressure is characterized by its large magnitude at very short impact duration (Plesset and Chapman, 1971) and goes along with the formation of a shock as well. For the other part, the liquid jet is associated with the formation of a stagnation pressure, which is of smaller amplitude but longer impact duration (Plesset and Chapman, 1971). The liquid jet hypothesis on the one hand is motivated by the assumption that near wall bubbles collapse under the influence of shock waves caused by the collapse of larger scale structures (Dular et al., 2006). A liquid micro-jet forms due to bubble-wall interaction (Plesset and Chapman, 1971) and impinges the solid surface. The jet is supposed to cause erosion pit formation if the liquid mass velocity exceeds a critical threshold velocity (Lush, 1983). An important foundation of the shock wave hypothesis on the other hand is the potential energy hypothesis initiated by Hammitt (1963). According to the later formulation by Vogel and Lauterborn (1988), it states that the potential energy of the spherical bubble is proportional with its initial volume and the difference between static ambient and vapor pressure. Vogel and Lauterborn (1988) further support the potential energy hypothesis by showing experimentally that the energy of a spherical acoustic transient as derived by Cole (1948) is proportional with the initial potential energy of a spherical bubble collapsing close to a solid wall. Although this strict linear relation has been shown to be valid for spherical bubbles only (Vogel and Lauterborn, 1988), we assume in this study that the collapse induced shock impact is the main contributor to surface damage for cavitating structures on the macroscopic scale.

Early applications of the potential energy concept to cavitating flow problems are found in the work by Pereira et al. (1998), Fortes Patella and Reboud (1998) and Fortes Patella et al. (2004). They explain how energy is transferred from the collapse of macroscale cavities to the solid surface in an energy cascade. As shown by Vogel and Lauterborn (1988) and Kato et al. (1996), the distance of imploding cavities from the impacted surface plays a major role in this energy cascade. Two different integral approaches have evolved from this understanding. One approach attempts to identify isolated collapse events to assess their surface impact strength from the wall distance and kinematic parameters. Mihatsch et al. (2015) partially assess the impact aggressiveness from the maximum local velocity divergence at the final stage of the collapse. Based on the work by Bark et al. (2004), Arabnejad and Bensow (2017) assess the collapse aggressiveness from the maximum volume change of the entire isolated cavity, which occurs prior to the final stage of the collapse. Another family of approaches rather attempts to assess the collapse strength in a direct integral fashion without isolating individual collapse events. Different from the approaches by Mihatsch et al. (2015) and Arabnejad and Bensow (2017), it is assumed that the collapsing cavities release their potential energy instantaneously during the collapse. Fortes Patella et al. (2012) integrate the locally released potential power over an aggressiveness height derived from the work by Kato et al. (1996). Leclercq et al. (2017) have derived a discrete surface impact power model from the solid angle projection of released power on a discrete surface element.

We consider the latter approach, also referred to as the cavitation intensity approach (Leclercq et al., 2017), as a suitable model for engineering purposes, because it is strongly linked to the cavity collapse kinematics, which are rather accurately predicted by commonly used mass transfer models, and because it directly accounts for the effects of wall distance, volume change and surface orientation relative to the imploding cavity. The cavitation intensity model is rewritten in a fully continuous form (Schenke and van Terwisga, 2018), which directly gives the local surface specific impact power without the necessity to reconstruct the solid angle as used by Leclercq et al. (2017). This impact power is then used to assess the risk of cavitation erosion. Common erosion risk indicators are obtained from the accumulation or integration of local impact events over time, where the individual event is only taken into account if it exceeds a certain threshold level. Examples are found in the work by Li et al. (2014) and Leclercq et al. (2017). This means, however, that above the pre-defined threshold level, the collapse rapidness is not further taken into account. A way to account for the rapidness of collapse events by exponential model parameters rather than a threshold definition is proposed by Nohmi et al. (2008). The physical meaning of the model parameters, however, has not further been specified. For this reason, a technique is introduced in this study to compute a weighted averaged impact power, where the extreme value of an impact signal is approached to a degree specified by an intensity exponent. Two slightly different impact power functions are derived to compute the averaged impact power. The response behavior of the two impact power functions is first tested for a systematic variation of a simple but representative manufactured signal. The approach is applied to the collapse of idealized cavities on a solid wall to investigate the effect of cavity shape and surface orientation on the collapse aggressiveness. An analytical prediction on the total amount of accumulated surface energy is derived from the cavitation intensity model. The amount of accumulated energy obtained from the numerical simulation is verified against the analytical prediction. The new aggressiveness indicators are further employed to assess the aggressiveness of the cavitating flow around a NACA0015 hydrofoil. Van Rijsbergen et al. (2012) have identified locations of high erosion risk for this configuration from experimental paint tests. Numerical erosion risk assessment for this case has been carried out by Li et al. (2014).

2. Modeling of cavitation intensity

2.1. Cavitating flow modeling

The flow model is a modified version of the flow solver interPhaseChangeFOAM available in the open source CFD package OpenFOAM (2018). Since bubble collapse and sheet cavitation dynamics have been shown to be mostly inertia driven on the macroscopic scale (Schmidt et al., 2009) and since only the cavitation dynamics are of interest in this study, the flow is assumed to be inviscid and the Euler equations for momentum and mass continuity are solved:

$$\frac{\partial}{\partial t}(\rho \mathbf{u}) + \nabla \cdot (\rho \mathbf{u} \otimes \mathbf{u}) = -\nabla p \tag{1}$$

$$\frac{\partial \rho}{\partial t} + \nabla \cdot (\rho \mathbf{u}) = 0 \tag{2}$$

In Eqs. (1) and (2), $\mathbf{u}$ is the mixture flow velocity, p the total pressure of the mixture and ρ the mixture density. The flow is assumed to be incompressible in the pure liquid and vapor phase, where ρ_l and ρ_v are the liquid and vapor density, respectively. The mixture density ρ is expressed in terms of the liquid volume fraction γ by the linear mixture relation

$$\rho = \gamma\rho_l + (1-\gamma)\rho_v, \qquad \text{where} \qquad 0 \leq \gamma \leq 1. \tag{3}$$

With p_v being the vapor pressure, the mass transfer model by Merkle et al. (1998) is employed in a slightly modified form (Schenke and van Terwisga, 2017) to model cavitation:

$$\nabla\cdot\mathbf{u} = -\frac{1}{\rho}\left(\frac{1}{\rho_v}-\frac{1}{\rho_l}\right)(p-p_v)\begin{cases} C_v\gamma & \text{if} \quad p \leq p_v \\ C_c(1-\gamma) & \text{if} \quad p > p_v \end{cases} \tag{4}$$

Different from the original implementation in OpenFOAM (2018), the source term is divided by the mixture density ρ. C_v and C_c are model coefficients to adjust the source term magnitude for the evaporation and condensation process, respectively. In its essence, the modified formulation helps to more efficiently distribute the mass transfer magnitude over the phase transition regime (Schenke and van Terwisga, 2017) and to keep the density-pressure trajectories close to vapor pressure during phase transition. Thereby, the conditions of more realistic thermodynamic equilibrium models are mimicked (Koukouvinis and Gavaises, 2015), even though unique equilibrium states cannot be achieved with this approach (Schenke and van Terwisga, 2017). Substituting the mixture density given by Eq. (3) into Eq. (2) gives the mass continuity equation expressed in terms of the liquid volume fraction:

$$\frac{\partial\gamma}{\partial t} + \nabla\gamma\cdot\mathbf{u} + \gamma\nabla\cdot\mathbf{u} = -\nabla\cdot\mathbf{u}\frac{\rho_v}{\rho_l-\rho_v} \tag{5}$$

Substituting the divergence term $\nabla\cdot\mathbf{u}$ on the right-hand side of Eq. (5) by Eq. (4) yields the transport equation of γ, which must be solved to achieve phase transition:

$$\frac{\partial\gamma}{\partial t} + \nabla\cdot(\gamma\mathbf{u}) = -\frac{1}{\rho\rho_l}(p-p_v)\begin{cases} C_v\gamma & \text{if} \quad p \leq p_v \\ C_c(1-\gamma) & \text{if} \quad p > p_v \end{cases} \tag{6}$$

2.2. Cavitation intensity model

The potential energy of an isolated spherical bubble of initial radius R_0 is given by the product of the initial bubble volume and the driving pressure difference (Vogel and Lauterborn, 1988), such that

$$E_{\text{pot,b}} = \frac{4}{3}\pi R_0^3(p_d - p_v), \tag{7}$$

where, in this case, p_d is the far away ambient pressure driving the bubble collapse. Because of the linearity of equation (7) with respect to the bubble volume $4/3\pi R_0^3$, the potential energy of an arbitrarily shaped cavity can be approximated by a continuous distribution of the volume specific energy e_{pot}, such that the total potential energy of the cavity follows from the volume integration of that distribution. The volume specific energy is proportional with the vapor volume fraction, such that $e_{\text{pot}} = (1-\gamma)(p_d - p_v)$ (Flageul et al., 2012). The change of volume specific potential energy is given by the material derivative of e_{pot}, written as

$$\frac{De_{\text{pot}}}{Dt} = -(p_d-p_v)\frac{D\gamma}{Dt} + (1-\gamma)\frac{Dp_d}{Dt}, \qquad \text{where} \quad \frac{D}{Dt} \equiv \frac{\partial}{\partial t} + \mathbf{u}\cdot\nabla. \tag{8}$$

Careful interpretation of Eq. (8) is needed when deriving the power radiated from a specific location. It is assumed that volume specific energy is released instantaneously if and only if condensation takes place. This implies that only the first term on the right-hand side of Eq. (8) contributes to the radiated power, and only if the material derivative of γ is positive. With the positive material derivative of γ denoted by $(D\gamma/Dt)^+$, the radiated power is given by

$$\frac{\partial e_{\text{rad}}}{\partial t} = \left(\frac{D\gamma}{Dt}\right)^+(p_d - p_v). \tag{9}$$

From the definition of the material derivative in Eq. (8) and from Eq. (5) follows that (Schenke and van Terwisga, 2018)

$$\left(\frac{D\gamma}{Dt}\right)^+ = \max\left[-\nabla\cdot\mathbf{u}\left(\gamma + \frac{\rho_v}{\rho_l-\rho_v}\right), 0\right]. \tag{10}$$

An equivalent of Eq. (9) in terms of vapor volume fraction as well as an equivalent of Eq. (10) in terms of density change is found in the work by Flageul et al. (2012). Since the change of potential energy resulting from the second term on the right-hand side of Eq. (8) occurs at constant specific volume, it cannot contribute to the conversion into radiated energy. However, the change of driving pressure throughout the cavity collapse is still reflected by the change of p_d in the first term on the right-hand side of Eq. (8). This is explained by following an associated Lagrangian particle and by expanding p_d in time using a first order Taylor series approximation in the Lagrangian reference frame, which is given by

$$\begin{aligned} p_d^{\mathfrak{L}}(t+\Delta t) &= p_d(t) + \left.\frac{Dp_d}{Dt}\right|_t \Delta t + \mathcal{O}\left(\Delta t^2\right) \\ &= p_d(t) + \left.\frac{\partial p_d}{\partial t}\right|_t \Delta t + \mathbf{u}\cdot\nabla p_d|_t \Delta t + \mathcal{O}\left(\Delta t^2\right). \end{aligned} \tag{11}$$

The superscript $\mathfrak{L}$ on the left-hand side of Eq. (11) indicates that the Taylor series expansion is carried out in the Lagrangian reference frame. The second term on the right-hand side of Eq. (11) represents the change of driving pressure due to the unsteadiness of the driving pressure field and the third term represents the change of driving pressure experienced by an associated Lagrangian particle as it moves along the driving pressure gradient. This interpretation of the driving pressure reflects that it is thought of as an ambient condition which the associated Lagrangian particle is subjected to, rather than a material property transported by the particle. A typical situation to further illustrate this interpretation is given by a vapor bubble collapsing towards the pressure recovery region around the trailing edge of a hydrofoil. As far as the change of potential energy according to Eq. (8) is concerned, the increase of driving pressure and the reduction of bubble volume counteract each other. Eq. (9), however, suggests that the instantaneous power radiation is only caused by the volume reduction at the instantaneous driving pressure difference $p_d - p_v$. As described by Eq. (11), the pressure recovery then reflects in the increase of p_d over time experienced by the moving bubble, and thus enhances the power radiation from the collapsing bubble.

It is assumed that the radiated energy propagates infinitely fast in radial direction from each point source and that the energy flux is not disturbed by the presence of other cavities. It is transformed into surface impact power such that the total amount of energy is conserved. Leclercq et al. (2017) propose a discrete model that involves the conversion of locally emitted energy into local surface impact power based on the solid angle projection on a triangular surface element as derived by van Oosterom and Strackee (1983). To avoid the necessity to project the radiated power on triangular surface elements, a fully continuous form of the model is introduced, which can then be applied to a finite grid in a more straight forward fashion. The surface specific impact power according to this formulation is given by

$$\left.\frac{\partial e_S}{\partial t}\right|_{\dot\gamma} = \frac{1}{4\pi}\left(\frac{\mathbf{x}\cdot\mathbf{n}}{|\mathbf{x}|^3}\right)\frac{\partial e_{\text{rad}}}{\partial t} \tag{12}$$

for a point source, indicated by the subscript $\dot\gamma$. With $\mathbf{x}_P$ being the position of the point source and $\mathbf{x}_S$ the impacted surface location,

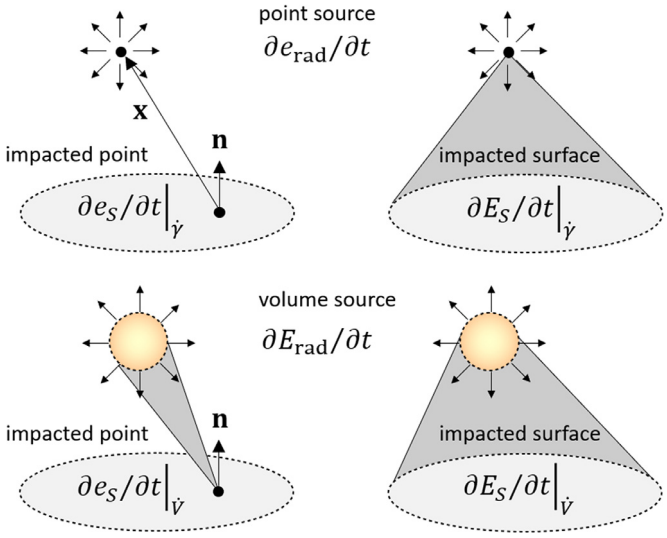

Fig. 1. Terminology of energy time derivatives.

the position of the point source **x** relative to the impacted surface location as used in Eq. (12) is defined as $\mathbf{x} = \mathbf{x}_P - \mathbf{x}_S$. Volume integration of Eq. (12) over the continuous source distribution yields the surface specific impact power resulting from a volume source as depicted in Fig. 1, indicated by the subscript $\dot{V}$:

$$\left.\frac{\partial e_S}{\partial t}\right|_{\dot{V}} = \int_{\text{vol}} \left.\frac{\partial e_S}{\partial t}\right|_{\dot{\gamma}} dV \equiv \dot{e}_S, \quad \text{where} \quad \dot{e}_S = \dot{e}_S(t, \mathbf{x}_S) \tag{13}$$

In the further course of the study, the simplified notation $\dot{e}_S$ introduced in Eq. (13) always refers to the instantaneous surface specific impact power at the surface location $\mathbf{x}_S$ caused by a volume source. When applied to a finite grid, Eq. (13) can directly be evaluated at the associated surface face center, irrespective of the face geometry. In spherical coordinates $(r,\ \theta,\ \varphi)$, we get $\mathbf{x}\cdot\mathbf{n} = r\sin\theta$ and surface integration of the bracket term in Eq. (12) gives

$$\int_{\text{surf}} \frac{\mathbf{x}\cdot\mathbf{n}}{|\mathbf{x}|^3} dS = \int_{\Delta\varphi}\int_{\Delta\theta} \sin\theta d\theta d\varphi \equiv \Omega, \tag{14}$$

which is the solid angle Ω as used in the work by Leclercq et al. (2017). By employing Eqs. (12) and (13) to directly evaluate the surface specific impact power at the face center, however, the reconstruction of the solid angle is not needed anymore. The instantaneous surface integrated impact power caused by a point source and volume source respectively is given by

$$\left.\frac{\partial E_S}{\partial t}\right|_{\dot{\gamma}} = \int_{\text{surf}} \left.\frac{\partial e_S}{\partial t}\right|_{\dot{\gamma}} dS \quad \text{and} \quad \left.\frac{\partial E_S}{\partial t}\right|_{\dot{V}} = \int_{\text{surf}} \left.\frac{\partial e_S}{\partial t}\right|_{\dot{V}} dS, \tag{15}$$

where again the subscript $\dot{\gamma}$ indicates the impact from a local point source and the subscript $\dot{V}$ the impact from the integrated volume source as shown in Fig. 1. For a closed convex surface we have $\Delta\theta = \pi$, $\Delta\varphi = 2\pi$ and hence $\Omega = 4\pi$. From Eq. (12) then follows that all the power released from the point source is impacting the surface. For a point source impacting a flat surface stretched to infinity, the overall surface integrated impact rate can be expressed in polar coordinates $(r_s,\ \varphi)$ as depicted in Fig. 2. Let the source be located at an arbitrary height h_s above the surface such that $\mathbf{x}\cdot\mathbf{n} = h_s$ and $|\mathbf{x}|^2 = r_s^2 + h_s^2$. The local impact rate then becomes

$$\left.\frac{\partial e_S}{\partial t}\right|_{\dot{\gamma}} = \frac{1}{4\pi} \frac{h_s}{\left(r_s^2 + h_s^2\right)^{\frac{3}{2}}} \frac{\partial e_{\text{rad}}}{\partial t}. \tag{16}$$

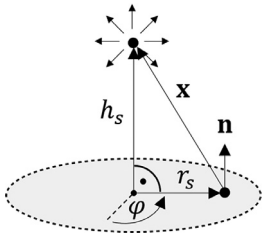

Fig. 2. Point source impacting a flat surface stretching to infinity.

Surface integration of Eq. (16) gives

$$\begin{aligned}\left.\frac{\partial E_S}{\partial t}\right|_{\dot{\gamma}} &= \int_0^{\infty}\int_0^{2\pi} \left.\frac{\partial e_S}{\partial t}\right|_{\dot{\gamma}} r_s d\varphi dr_s \\ &= \frac{h_s}{2}\frac{\partial e_{\text{rad}}}{\partial t}\int_0^{\infty} \frac{r}{\left(r_s^2 + h_s^2\right)^{\frac{3}{2}}} dr_s = \frac{1}{2}\frac{\partial e_{\text{rad}}}{\partial t}.\end{aligned} \tag{17}$$

Since Eq. (17) holds for any arbitrary point source in the domain, we get (Schenke and van Terwisga, 2018)

$$\int_{\text{flat surf}} \left.\frac{\partial E_S}{\partial t}\right|_{\dot{V}} dS = \frac{1}{2}\frac{\partial E_{\text{rad}}}{\partial t}. \tag{18}$$

The intuitive result from Eq. (18) is that half of the emitted potential cavity energy is eventually distributed on the flat surface, irrespective of the cavity shape, orientation and initial distance from the impacted surface. However, the latter three aspects may have strong influence on how this same total amount of energy is distributed and focused on the surface, both in space and time.

2.3. Finite grid representation

On a finite grid, all quantities in Eqs. (9) and (10) which are needed to compute the volume specific power radiated from a specific location are evaluated at the cell centers, except for the velocity divergence $\nabla\cdot\mathbf{u}$, which is reconstructed from the face fluxes. The distance **x** between the source and the impact location in Eq. (12) is given by the distance between the cell center of the source and the face center of the impacted surface face. The face normal vector **n** is given at the face center as well. The volume integration over all sources contributing to one surface impact location (see Eq. (13)) is done by multiplying the locally radiated volume specific energy by the corresponding cell volume V_c and by summation over all contributing cells. It is noted that the emitting grid cell of volume V_c can be thought of as a sphere of the same volume, which gives an equivalent radius $r_{\text{eq}} = [3V_c/(4\pi)]^{1/3}$. The radiated power is then given by a corresponding flux across the sphere surface. It is assumed that the spatial resolution on the final grid is limited by r_{eq}. This means that near wall grid cells are treated such that the distance $|\mathbf{x}|$ from the impact location in Eq. (12) is substituted by the equivalent sphere radius if $|\mathbf{x}| < r_{\text{eq}}$. The surface integrated impact power given by Eq. (15) is obtained by multiplying the local surface specific impact power with the corresponding face area and by summation over all surface faces. Further multiplying the instantaneous surface integrated impact power with the time step size Δt and summing up over all time steps gives the accumulated surface energy E_S. In case of a flat surface large enough to be considered as infinite with respect to the impacting cavity and further assuming that the driving pressure p_d is constant throughout the cavity collapse, it follows from Eq. (18) that the amount of accumulated surface energy must be half of the initial potential cavity energy $E_{\text{pot},0}$, such that $E_S = 1/2 E_{\text{pot},0}$. The accumulated surface integrated energy E_S obtained from the numerical simulation can be verified against this theoretical value.

2.4. Weighted averaged impact power

The collapse aggressiveness is assessed by weighted averages of the local surface specific impact power obtained from the cavitation intensity model. The technique amplifies the extreme events to an extent specified by an intensity exponent n. It is first noted that the accumulated surface specific energy e_S at some surface location $\mathbf{x}_S$ and after some sample time $t^* > 0$ is given by

$$e_S(t^*, \mathbf{x}_S) = \int_0^{t^*} \dot{e}_S(t, \mathbf{x}_S) dt. \tag{19}$$

As another interim step, the impact intensity exponent n is introduced to amplify the impact rate, which is then integrated over the surface specific energy, such that

$$\int_{e_S(0,\mathbf{x}_S)}^{e_S(t^*,\mathbf{x}_S)} \{\dot{e}_S(t, \mathbf{x}_S)\}^n de_S(t, \mathbf{x}_S) = \int_0^{t^*} \{\dot{e}_S(t, \mathbf{x}_S)\}^{n+1} dt. \tag{20}$$

Two weighted impact power functions are derived from Eq. (20). The first function is normalized by the accumulated surface specific energy:

$$\langle \dot{e}_S \rangle_{e_S} = \left[\frac{1}{e_S(t^*, \mathbf{x}_S)} \int_0^{t^*} \{\dot{e}_S(t, \mathbf{x}_S)\}^{n+1} dt \right]^{\frac{1}{n}} \tag{21}$$

The second function is obtained by normalizing Eq. (20) by the sample time t^*:

$$\langle \dot{e}_S \rangle_f = \left[\frac{1}{t^*} \int_0^{t^*} \{\dot{e}_S(t, \mathbf{x}_S)\}^{n+1} dt \right]^{\frac{1}{n+1}} \tag{22}$$

The exponents $1/n$ and $1/(n+1)$ are introduced for the function values to have the physical dimension of surface specific power. The response behavior of the two functions given by Eqs. (21) and (22) is inspected by means of a manufactured signal. A representative signal is constructed from two rectangular signals of different amplitudes (also see Fig. 3), associated with a base signal of continuous energy intake and a short high amplitude pulse, respectively:

$$\dot{e}_S = \begin{cases} \hat{e}_S & \text{if} \quad 0 \le t \le \delta t \quad (\textit{pulse signal}) \\ \alpha \hat{e}_S & \text{if} \quad \delta t < t \le k\delta t \quad (\textit{base signal}) \end{cases}$$
$$\textit{where} \quad k\delta t = t^*, \quad k \ge 1 \quad \textit{and} \quad 0 \le \alpha \le 1 \tag{23}$$

In this case, the two impact power functions given by Eqs. (21) and (22) can be rewritten as

$$\langle \dot{e}_S \rangle_{e_S}^m = \hat{e}_S \left[\frac{1 + (k-1)\alpha^{n+1}}{1 + (k-1)\alpha} \right]^{\frac{1}{n}} \tag{24}$$

and

$$\langle \dot{e}_S \rangle_f^m = \hat{e}_S \left[\frac{1 + (k-1)\alpha^{n+1}}{k} \right]^{\frac{1}{n+1}}, \tag{25}$$

respectively, where the superscript m refers to the manufactured signal given by Eq. (23). The parameter n is still the only model parameter, whereas k and α only change the characteristics of the manufactured signal. The manufactured signal can be thought of as periodic, with t^* being the period. The pulse duration relative to the base signal period decreases with increasing k and the amplitude ratio between the base and the pulse signal is given by α. Figs. 4 and 5 depict response surfaces of the impact power functions given by Eqs. (21) and (22) applied to the manufactured signal for a systematic variation of α and k and for different values of the intensity exponent n. Both functions tend to return the peak value of the power impact signal as the intensity exponent n increases, given that the duration of the pulse relative to the characteristic signal period is finite. If the relative pulse duration approaches 0 and n is finite, however, both functions return the amplitude $\alpha\hat{e}_S$ of the base signal. This regime is identified by equidistant horizontal iso-lines of the response surfaces in Figs. 4 and 5. The most significant difference in response behavior occurs for small values of α in combination with small values of n. In this case, the function $\langle \dot{e}_S \rangle_{e_S}$ given by Eq. (21) generally tends to return larger values than the function $\langle \dot{e}_S \rangle_f$ given by Eq. (22). In the limit $n \to 0$, $\langle \dot{e}_S \rangle_f$ represents the accumulated surface energy $e_S(t^*)$ per sample time t^*, whereas $\langle \dot{e}_S \rangle_{e_S}$ still tends to return the pulse amplitude of a signal as long as the energy accumulated by the pulse is significantly larger than the energy accumulated from the low amplitudes. The same applies to the limit $\alpha \to 0$. The impact power function $\langle \dot{e}_S \rangle_{e_S}$ given by Eq. (21) is specifically designed to

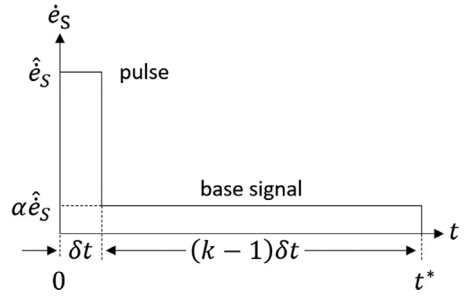

Fig. 3. Manufactured signal with $0 \le \alpha \le 1$ being a measure for the base signal amplitude relative to the pulse signal amplitude and k being a measure for the base signal duration relative to the pulse duration.

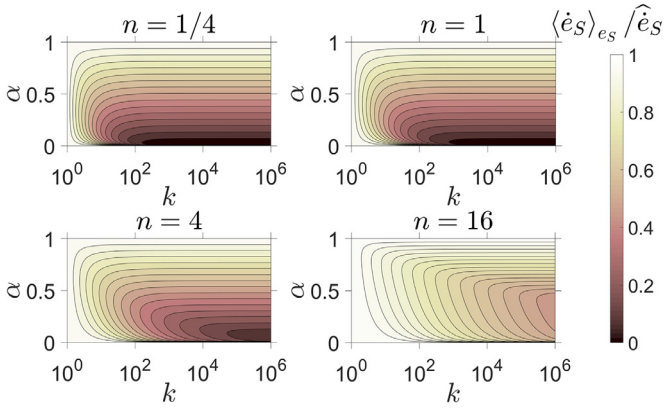

Fig. 4. Response surfaces to the manufactured signal in Fig. 3 obtained from the impact power function $\langle \dot{e}_S \rangle_{e_S}$ given by Eq. (21) for different values of the intensity exponent n.

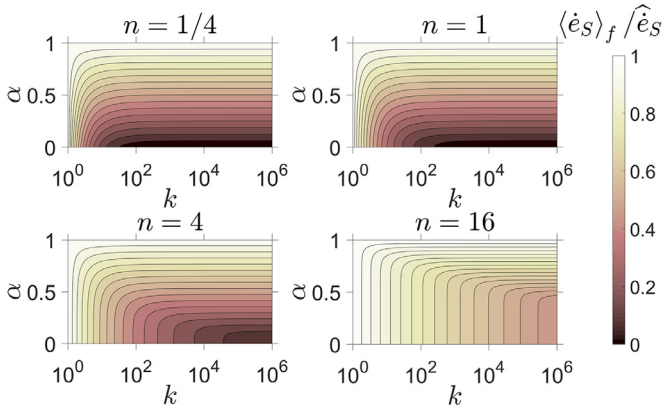

Fig. 5. Response surfaces to the manufactured signal in Fig. 3 obtained from the impact power function $\langle \dot{e}_S \rangle_f$ given by Eq. (22) for different values of the intensity exponent n.

assess the aggressiveness of individual events on the one hand, because it does not change its function value over times where no further energy is accumulated. The aggressiveness of periodic cavitating flows on the other hand can be assessed by both the $\langle \dot{e}_S \rangle_{e_S}$ function and the $\langle \dot{e}_S \rangle_f$ function. Thus, the choice of the impact power function as well as the value of the intensity exponent n depends on whether the aggressiveness of the flow is supposed to be related to individual extreme events or rather the amount of accumulated energy at a specific surface location.

2.5. Effective driving pressure

The largest uncertainty in the cavitation intensity approach concerns the modeling of the driving pressure p_d effectively driving the cavity collapse. This quantity is typically unknown in complex flow situations. An example would be the cavitating flow around a hydrofoil or any other obstacle, where pressure recovery gradients along the obstacle are important for the dynamics of the cavitating flow. For a bubble collapsing close to a solid wall, the driving pressure across its interface varies due to the effect of wall interaction, leading to deformation of the bubble and, in last instance, to the formation of a liquid jet impacting the wall (Plesset and Chapman, 1971). Even for an isolated bubble, the presence of the hydrostatic pressure gradient leads to deformation at a certain stage of the collapse (Obreschkow et al., 2011). Thus, the driving pressure is practically never exactly constant in space. The local cell pressure p cannot be used as an estimate of the driving pressure, because the driving pressure must be computed at the same locations $\mathbf{x}_P$ where energy is radiated. Since the radiated power is proportional with the negative velocity divergence (see Eqs. (9) and (10)), the corresponding pressure difference $p - p_v$ would be nearly zero because the density-pressure trajectory evolves very close to vapor pressure during phase transition. An approach to determine the driving pressure in complex flow situations is suggested and implemented by Arabnejad and Bensow (2017). In their work, coherent cavition structures are identified and simplified to an equivalent isolated spherical bubble of equivalent volume. Thus, the driving pressure can be determined from the Rayleigh–Plesset equation (see Rayleigh, 1917 and Plesset, 1949) and a set of kinematic parameters uniquely defining the state of the collapse (Bark et al., 2004), however at the cost of not reflecting the exact shape of the collapsing structure and its orientation relative to the impacted surface. Since both cavity shape and surface orientation were demonstrated to affect the collapse aggressiveness (Van Rijsbergen et al., 2012), we take both effects into account by determining the energy release of the collapsing cavity from the cell level. Since coherent structures are neither isolated nor simplified to spherical bubbles, however, the driving ambient pressure cannot be derived from bubble dynamics considerations in this case. In cyclic flows with steady state inflow conditions, the time averaged pressure distribution

$$\langle p \rangle_t = \frac{1}{t^*} \int_0^{t^*} p(t, \mathbf{x}_P) dt \tag{26}$$

provides at least an approximation of the conditions which collapsing cavities meat on statistical average (see Schenke and van Terwisga, 2018; Melissaris et al., 2018). The time averaged pressure under cavitating flow conditions is employed as the driving pressure field in the hydrofoil test case, in which the cavities are shed into a pronounced pressure recovery gradient towards the trailing edge. This study is restricted to a steady driving pressure field at steady inflow conditions, obtained from a sample time t^* that theoretically approaches infinity. The driving pressure is calculated in the entire domain prior to the application of the cavitation intensity model and it is evaluated at the same locations $\mathbf{x}_P$, where also the radiated power is computed. A more instantaneous approximation of the driving pressure field can be achieved by shorter sample times, which must be small enough to reflect the characteristic flow frequency, and large enough to filter out individual collapse peak pressures.

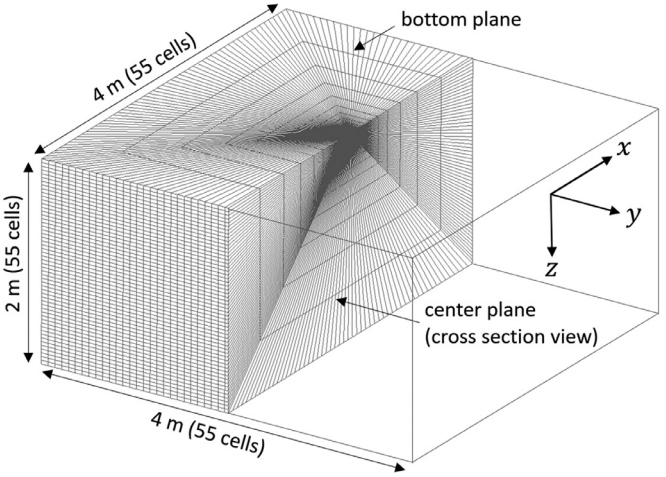

Fig. 6. Second finest grid in Table 1 with the 4 m × 4 m solid bottom plane.

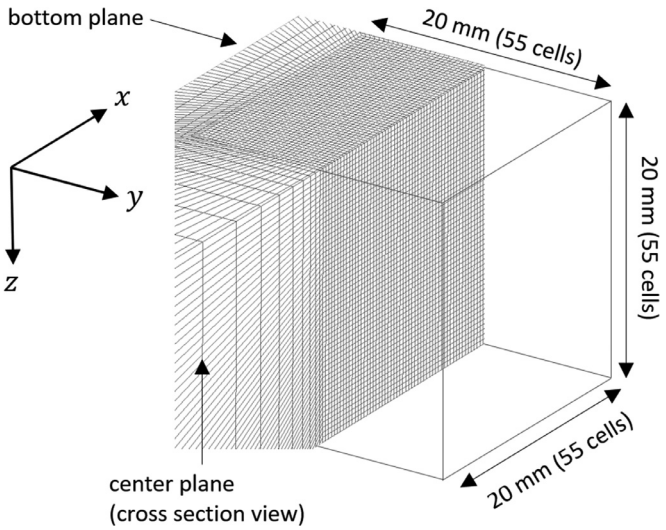

Fig. 7. Detail of the cubic inner domain of the second finest grid in Table 1.

3. Numerical test cases

3.1. Idealized cavities

The first study serves as a verification study and concerns the collapse of idealized cavity types on a flat bottom surface as depicted in Fig. 8. The wall surface area is 4 m by 4 m (see Fig. 6), large enough to verify whether 50% of the initial potential cavity energy is transmitted to the surface as predicted from Eq. (18). Next to the verification study, the effect of cavity shape on the collapse aggressivness is investigated. The investigated shapes are basically a bubble and a ring cavity. In one case, a bubble with a radius of $R_b = 3.84$ mm collapses in near wall distance $h = 0.5$ mm and in another case the same bubble is cut in half such that it forms a hemisphere directly collapsing on the solid surface. Similarly, a ring cavity collapses parallel to the wall at the same distance h in one case. In the final case, the torus is cut in half and rotated by 90 degrees such that it forms a horseshoe type cavity with its legs perpendicular on the solid surface. The initial torus

Table 1
Grid densities of the inner domain (see Fig. 7) and the corresponding deviation of the finite grid horseshoe volume $V_{h,\text{grid}}$ from the theoretically exact horseshoe volume $V_{h,\text{th}} = \pi^2 r_t^2 R_t$, measured by the error $\epsilon = \left(V_{h,\text{grid}} - V_{h,\text{th}}\right)/V_{h,\text{th}}$.

N_{cells}/length	N_{cells} total	Volume off-set
65/0.02 m^{-1}	802,750	−0.38%
55/0.02 m^{-1}	544,500	−0.46%
45/0.02 m^{-1}	344,250	−0.68%
35/0.02 m^{-1}	196,000	−1.06%
25/0.02 m^{-1}	93,750	−1.94%
15/0.02 m^{-1}	31,500	−5.15%
5/0.02 m^{-1}	3250	−38.79%

radius of the ring cavity is $R_t = 6$ mm and the corresponding tube radius is $r_t = 2$ mm, such that the initial horsehsoe cavity volume is equal to the initial bubble volume. Consequently, the initial ring cavity volume is twice the initial bubble volume and the initial hemisphere volume is half of the initial bubble volume. In addition, an isolated bubble collapse without wall interaction provides a reference solution which is verified against the analytical solution of the Rayleigh–Plesset equation (see Rayleigh, 1917 and Plesset, 1949) in the absence of viscous and surface tension forces. The solid wall of the hemisphere case is replaced by a symmetry plane in this case.

It is emphasized that the results of this study cannot directly be compared to real world situations, where similar structures may appear, however under different ambient conditions which are not reflected in this study. Most significantly, all cavities are initialized with the flow being at rest, whereas the dynamics of cavitating ring structures are a result of circulation and vorticity in the flow field (see Kawanami et al., 2002; van Terwisga et al., 2009; Dular and Petkovšek, 2015). On the one hand, the vorticity in the vicinity of a collapsing cavitating vortex ring has a damping effect on the driving pressure field (Chahine and Genoux, 1983) and hence on the collapse aggressiveness. On the other hand, cavitating horseshoe vortices typically occur under flow conditions that cause a break-up of the cavitating horseshoe vortex at the top (Kawanami et al., 2002). This break-up is supposed to enhance the erosive aggressiveness because the horseshoe legs are then more efficiently collapsed towards the surface (see van Terwisga et al., 2009; Dular and Petkovšek, 2015). Both of the previous effects are not present in the simulation and only the effect of initial shape and surface orientation relative to the imploding ring cavity can be studied. Furthermore, the initial vapor volume fraction of all cavities is chosen to be 1, although the cavitating ring structures are supposed to exhibit a lower fraction as they are presumably formed by clusters of vapor bubbles (van Terwisga et al., 2009). It is argued that the choice of the initial volume fraction does not affect the collapse time of the cavity as long as the associated bubble density is large enough to not allow for any significant pressure recovery in the liquid phase between the bubbles. However, according to the modeling approach presented in this study, the initial potential cavity energy and hence the accumulated surface energy is proportional with the initial vapor volume fraction. Therefore, the study should be seen as an artificial numerical experiment, designed to identify numerical error sources involved in the conversion of potential energy into local impact power and to isolate the effects of cavity shape and surface orientation relative to the imploding cavity on the collapse aggressiveness.

The mesh is block structured and the inner part of the domain consists of cubic cells uniformly distributed in a cube. Just as in the bubble cluster collapse simulation by Schmidt et al. (2011), the cube edge length is 0.02 m (see Fig. 7). A systematic variation of time step size Δt is carried out for the horseshoe cavity to identify the temporal resolution at which the cavity collapse time becomes time step size independent. In order to carry out a grid sensitivity study, the grid density of the inner cubic part is varied from 5 cells per 0.02 m for the coarsest grid to 65 cells per 0.02 m for the finest grid (see Table 1). The number of cell layers connecting the inner part with the far field boundaries is kept constant at 25. The provided grid and time resolution resolves the collapse dynamics on a macroscopic scale. The cavities are initialized such that $\gamma = 0$ for those cells entirely located inside the cavities and $\gamma = 1$ for those entirely located outside the cavity. The corresponding densities of the vapor and the liquid phase are assumed to be $\rho_v = 0.02$ kg/m^3 and $\rho_l = 1000$ kg/m^3, respectively. The cut cell volume fraction is then given by the fraction by which the cell is occupied by the liquid phase, determined from a sample algorithm applied to the corresponding cell. The presence of cut-cells leads to inaccuracies in the representation of the initial cavity interface and also the initial cavity volume. Table 1 shows the initial volume off-set from the analytical correct value in percent for the seven grid densities investigated in this study. Negative values represent too small initial volumes. Since the flow is assumed to be inviscid, the slip wall boundary condition is applied to the velocity field at the solid bottom plane. At the far field boundaries, the velocity field is constrained by the zero gradient boundary condition. The zero gradient boundary condition is further applied to the liquid volume fraction field at all boundaries, whereas the pressure field is constrained by the zero gradient boundary condition at the solid bottom plane only. At the far field boundaries, a fixed value of $p_\infty = 1$ bar, associated with the driving pressure p_d, is imposed. The pressure field is initialized at $p_v = 2340$ Pa inside the cavities and $p_\infty = 1$ bar outside the cavities, where the cut cell pressure is obtained from linear interpolation over the cut cell volume fraction. With the flow being at rest initially, the pressure equation evolves into a Laplace equation for pressure, thereby providing a solution of the Laplace equation of pressure. The pressure equation is solved first to avoid unrealistic behavior in the volume fraction transport equation due to the sharp pressure jump at the cavity interface. For the cavity collapse test case, the mass transfer coefficients are chosen to be $C_c = C_v = 1000$ kg·s/m^5. From previous studies, this value was found to be large enough to keep the cavity interface sharp during the collapse (Schenke and van Terwisga, 2017). Gravitational forces are neglected, because the involved buoyancy effects act on a significantly larger time scale than the cavity collapse time in this case. All idealized cavities are initialized with the flow being at rest, even though the horseshoe cavity is a vortical structure in reality.

3.2. NACA0015 hydrofoil

The second test case involves the application of the aggressiveness indicators to the cavitating flow around a NACA0015 hydrofoil. Cord length and span of the foil are 0.06 m and 0.04 m, respectively. The dimensions of the tunnel cross section, the foil and its position and angle of attack are in line with an experimental set-up by Van Rijsbergen et al. (2012) and a corresponding numerical set-up by Li et al. (2014). The tunnel width is $w_t = 0.04$ m and equal to the foil span and the tunnel height is $h_t = 2w_t$, with the cord center of the foil located at half height. The tunnel length is $l_t = 0.57$ m (see Fig. 10). The study is carried out for a downstream ambient pressure of $p_\infty = 302.3$ kPa, a uniform horizontal inflow speed of 17.3 m/s and an angle of attack of $\beta = 8^\circ$ (see Fig. 13). The fixed value velocity boundary condition is specified at the inlet and the fixed value pressure boundary condition at the outlet as indicated in Fig. 10. In order to get rid of pressure fluctuations at the outlet boundary, the flow is diffused in a diffuser section, starting at 6.5 cord lengths downstream from the foil's leading edge. Since the flow is inviscid, mass continuity and

Table 2
Grid densities for the hydrofoil grid refinement study.

Grid nr.	Δx (finest level) [mm]	N_{cells} total
0	0.15625	1,794,140
1	0.31250	919,944
2	0.62500	393,096
3	1.25000	114,694

Bernoulli's equation can be used to determine the outlet pressure such that the aimed tunnel pressure p_∞ is obtained under wetted flow conditions and, on time average, under cavitating flow conditions (Schenke and van Terwigsa, 2017). The liquid volume fraction γ is constrained by a zero gradient boundary condition at all boundaries except for the inflow boundary, where a fixed value of $\gamma = 1$ is applied. The unstructured mesh as depicted in Fig. 12 includes four refinement levels. At each refinement level, the cell length is reduced by factors of 2^{-n} against the base mesh, where $n = 0$ on the base mesh level and $n = 4$ on the finest level. Variation of grid density is achieved by changing the number of cells in the base mesh. For all refinement levels and all grids, the characteristic cell aspects are $\Delta x = \Delta y = 0.5\Delta z$ with respect to the coordinate system depicted in Fig. 13. By this means, geometrically similar grids are obtained and a uniformly spaced grid is achieved in the cavitating region. Table 2 lists the characteristic longitudinal cell lengths Δx on the finest level for the four different grid configurations investigated in this study. The grid depicted in Fig. 12 corresponds to grid 1 from Table 2. The time step size Δt is systematically decreased until a physically converged solution is obtained. Since the dynamics of the larger scale cavitation structures are of primary interest in this study, the frequency of large pressure pulses, associated with the cyclic collapse of larger scale structures and hence the shedding frequency, is employed as a measure for physical convergence. The collapse frequency is obtained from power spectral density analysis of the pressure signals at two observation points upstream from the leading edge and two observation points downstream from the trailing edge. The corresponding coordinates in Table 3 are given with respect to the coordinate system depicted in Fig. 13. The phase transition behavior is monitored at observation point P_0 in Table 3, located on the foil surface at half span and 20% cord length as indicated in Fig. 11. From previous studies (Schenke and van Terwigsa, 2017), the values $C_c = 5000$ kg·c/m^5 and $C_v = C_c/2$ for the mass transfer coefficients have been found to be large enough to obtain model parameter independent results for the cavity shedding frequency. Just as in the study by Li et al. (2014), the vapor pressure is $p_v = 1854$ Pa and the densities of the vapor and the liquid phase are $\rho_v = 0.014$ kg/m^3 and $\rho_l = 998.85$ kg/m^3, respectively. This corresponds to a downstream cavitation number of $\sigma = 2.01$. Gravitational forces are taken into account, although they are presumably negligible. The temporal resolution needed to obtain a physically converged result for the cavitating flow dynamics has been found to be significantly larger than the temporal resolution needed to evaluate the instantaneous impact power from Eq. (13). For this reason, Eq. (13) as well as the impact power functions given by Eqs. (21) and (22) are evaluated at $5\Delta t$ for this test case to reduce the overall computation time.

3.3. Iterative and discretization schemes

A segregated pressure-based approach is applied to solve the equations. Pressure-velocity coupling is achieved by solving a pressure equation, involving a Laplacian term of the pressure field, followed by a correction of the velocity field which is directly obtained by forward substitution of the previously computed pressure field (Jasak, 1996). The pressure equation and the velocity correction step provide a solution of the Euler equations given by Eqs. (1) and (2). Phase transition is achieved by solving the transport equation of liquid volume fraction given by Eq. (6). In all cases, the solver is run in a PISO mode as implemented in OpenFOAM (see Jasak, 1996; OpenFOAM, 2018), which means that the liquid volume fraction transport equation, placed in the outer iteration loop, is solved once per time step only. Three inner iteration loops over pressure equation and velocity correction are performed. The global residual of the equations to be solved is given by the L_1 norm, involving normalization by the maximum coefficient of the corresponding matrix diagonal (Moukalled et al., 2015). The number of solution iterations for the γ-transport equation is chosen such that the final residual of the discretized γ-transport equation drops below 10^{-13}. The final residual tolerance of the pressure equation is 10^{-11}. No relaxation is applied. The finite volume method is employed for spatial discretization and a collocated grid arrangement is used. For discretization of the convective terms in the momentum equation and the liquid volume fraction transport equation, the upwind-biased linear scheme (Warming and Beam, 1975) and the van Leer (1974), respectively, is employed. The Laplacian term of pressure in the pressure equation is discretized by using a linear scheme as described in Jasak (1996). Time discretization is linear implicit, where the mass transfer source term is treated partially implicit in both the γ-transport equation and the pressure equation.

4. Results and discussion

4.1. Collapse of idealized cavities

4.1.1. Convergence study

Both the grid sensitivity and the time step study are carried out for the horseshoe cavity collapse only. The horseshoe is chosen as a reference because it has a larger surface area to volume ratio than a sphere and therefore imposes higher demands on spatial resolution. Fig. 14 depicts the evolution of dimensionless vapor volume during the cavity collapse in red lines. Lines of the same colour represent different time step sizes. Large time step sizes lead to significant delays of the cavity collapse due to insufficient temporal resolution of the event. As the time step size approaches $\Delta t = 10^{-7}$ s, the horseshoe collapse time converges to a time step size independent value.

Concerning the surface integrated energy, it was found that the theoretical value of $E_S = 1/2E_{\text{pot}}$ is not always correctly predicted from the simulation results. Table 4 lists the deviation from the theoretical value for nine configurations of time step size and grid density, where a negative sign indicates underprediction of the theoretically exact value. Interestingly, the deviation from the theoretical value increases when the grid is refined and/or more temporal resolution is provided, even if the cavity collapse time itself has converged to a grid and time step size independent value.

The source of this error was found to be the velocity divergence term $\nabla \cdot \mathbf{u}$. To isolate the error source, it is eliminated by correcting the velocity divergence field by a constant factor c. The constant c is determined such that the volume integrated rate of vapor destruction predicted from the material derivative $(D\gamma/Dt)^+$ given by Eq. (10) agrees with the rate of vapor destruction predicted from the partial time derivative $(\partial\gamma/\partial t)^+$, such that

$$c\int_{\text{vol}}\left(\frac{D\gamma}{Dt}\right)^+ dV = \int_{\text{vol}}\left(\frac{\partial\gamma}{\partial t}\right)^+ dV. \tag{27}$$

The corrected velocity divergence field $c\nabla \cdot \mathbf{u}$ is computed at each time step. This correction can be done in this particular case only because it is based on the volume change of the entire cavity. As there is only condensation involved during the cavity collapse, the

volume change cannot be subject to the cancellation of competing condensation and evaporation processes at different locations in the domain. For the same reason, the correction of the divergence field is not applicable to the hydrofoil test case.

The evolution of accumulated surface energy obtained from the corrected divergence field is depicted in Fig. 14 for different time step sizes. Now, the accumulated surface integrated energy converges to the theoretical value of 50% initial potential energy. A number of numerical error sources inherent with the mass transfer modeling approach (Ghahramani and Bensow, 2018) may contribute to an inconsistent prediction of the velocity divergence field, even if the velocity divergence is directly reconstructed from the face fluxes as done in this study. One possible reason is that the face values of **u** are the result of an interpolation from the cell centers due to the collocated grid arrangement. It is further recalled that the velocity divergence term on the right hand side of the liquid volume fraction transport Eq. (5) is modeled by the mass transfer source term. As shown by Ghahramani and Bensow (2018), this term is not necessarily equal to the velocity divergence term on the left-hand side. Ghahramani and Bensow (2018) explain this mismatch by the fact that the liquid volume fraction transport equation is solved in a separate step within the iterative numerical algorithm. They could show that spurious numerical errors resulting from this inconsistency are significantly reduced for the simulation of a single bubble collapse, if the volume fraction normally obtained from the transport equation is replaced by the exact solution obtained from the Rayleigh–Plesset equation (Ghahramani and Bensow, 2018). Against this background, it may even be argued that the partial time derivative of liquid volume fraction $\partial\gamma/\partial t$ might give more accurate results for the energy release than the conceptually correct material derivative $D\gamma/Dt$ reconstructed from the velocity divergence field, at least in situations where potentially aggressive events associated with rapid phase change occur.

The same sensitivity study on evolution of dimensionless vapor volume and accumulated surface energy is carried out for different grid densities. The evolution of vapor volume and accumulated surface energy shown in Fig. 15 indicate a small sensitivity of the cavity collapse time with respect to spatial resolution as long as the initial cavity shape and its volume is at least roughly resolved. This is just the case for a resolution of 15 cells/0.02 m. For finer grids, the cavity collapse time hardly changes anymore, even though the initial cavity volume for 15 cells/0.02 m deviates from the theoretical value by 5.2% (see Table 1). The only significant deviation of collapse time is observed for the coarsest grid. Due to the initialization algorithm, the lowest liquid volume fraction is larger than 0.5 in this case. Since the initial pressure field is determined from the initial volume fraction field by linear interpolation, the minimum pressure obtained inside the cavity is larger than 0.5 bar. This results in a significantly smaller driving pressure difference $p_d - p_v$, explaining the pronounced delay in collapse time despite the circumstance that the initial cavity volume is underestimated by 38.8%. The time step and grid sensitivity is further investigated for the instantaneous energy impact rate $\dot{e}_S$ on the surface. Fig. 16 depicts the evolution of the maximum impact rate $\dot{e}_{S,\max}$ recorded on the solid surface for different time step sizes. The location of the maximum value may vary over time. Very similar results are obtained for small time steps. For the smallest time step size $\Delta t = 10^{-7}$ s, a very short peak pulse is observed at the final collapse stage, which is not present for the larger time steps. For very large time steps, the maximum impact is more and more underestimated as the final stage of the cavity collapse is approached. A similar behavior is found for variation of the grid density. Fig. 17 shows that the evolution of the maximum impact rate converges with increasing grid resolution, indicating grid independent behavior.

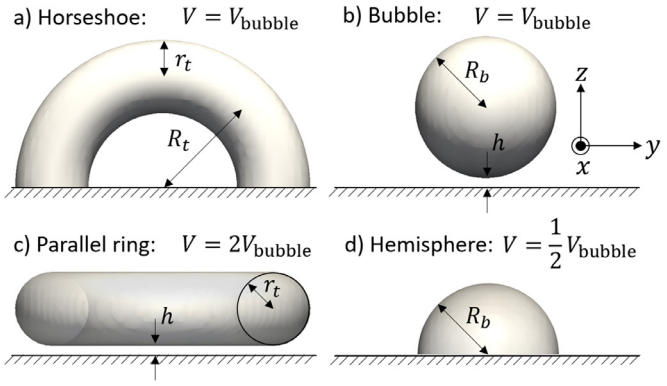

Fig. 8. Idealized cavity types ($\gamma = 0.5$ iso-surface) with $R_b = 3.84$ mm, $h = 0.5$ mm, $R_t = 6$ mm and $r = 2$ mm.

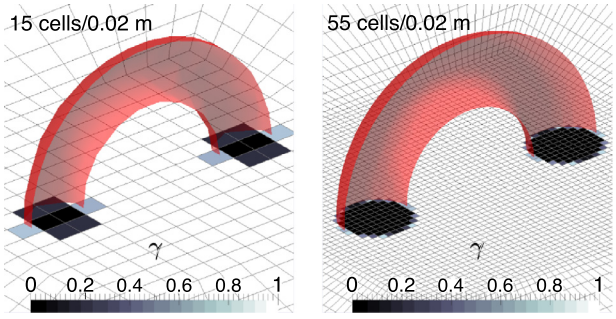

Fig. 9. Second coarsest (left) and second finest (right) grid from Table 1 and a $\gamma = 0.5$ iso-surface of the initial horseshoe cavity.

4.1.2. Physical analysis of the results

The evolution of the dimensionless cavity volume $V(t)/V_0$ as shown in Fig. 18 reveals pronounced differences in collapse time between the different cavity types. As a reference solution, Fig. 18 further depicts the vapor volume evolution of an isolated bubble collapsing in absence of a solid wall. The solution shows satisfactory agreement with the analytical solution obtained from the Rayleigh–Plesset equation (see Rayleigh (1917) and Plesset (1949)) under neglect of viscous and surface tension forces. The dimensionless volume evolution of the isolated bubble exactly coincides with the one of the hemisphere collapsing on the wall, implying that in this case the solid wall can be thought of as a symmetry plane of an isolated spherical bubble. In that sense, the hemisphere is not subjected to wall interaction action, at least not at the macroscopic scale and in the absence of viscous and surface tension forces. However, the effect of wall interaction causes the near wall bubble to collapse slower than the isolated bubble and the hemisphere. Similarly, it causes the parallel ring to collapse significantly slower than the horseshoe cavity, even though the initial torus and tube radius of both cavities are the same.

For the comparison of the impact aggressiveness, it is noted that the comparability of the results to real world situations is limited by the simplifying boundary and initial conditions as discussed in Section 3.1. It is only the effect of initial shape and surface orientation relative to the cavity in the absence of vorticity as well as surface tension and viscous forces that is reflected by the flow simulation. Fig. 20 shows the surface distribution of impact energy accumulated throughout the collapse of the horseshoe cavity, the near wall bubble, the parallel ring cavity and the hemisphere. The black solid line indicates the outline of the initial cavity shape. In this specific situation, the near wall bubble exhibits the largest efficiency to focus its potential energy on the surface, followed by the hemisphere, the horseshoe cavity and the parallel

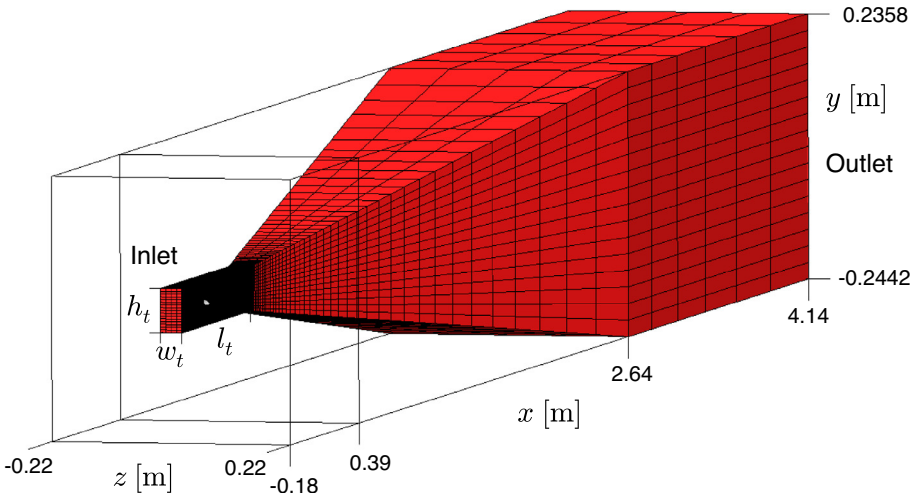

Fig. 10. Computational domain with downstream diffuser section for grid 1 from Table 2, the tunnel dimensions being $w_t = 0.04$ m, $h_t = 2w_t$ $l_t = 0.57$ m and the distance between leading edge and inlet 0.18 m.

ring cavity in order of decreasing maximum surface specific energy. The maximum values of accumulated surface specific energy appear to be close to each other for all cavities. However, the difference in initial cavity volume should be taken into account here. Also the influence of the initial wall distance h on the footprint caused by the near wall bubble and the parallel ring is not further investigated in this study.

A comparison of the averaged impact power distribution, measured by the averaged impact rate $\langle \dot{e}_S \rangle_{eS}$ given by Eq. (21) for $n = 1.0$, is presented in Fig. 21. This figure indicates the most focused impact distribution for the hemisphere, followed by the horseshoe cavity, the bubble and the parallel ring. The different ranking compared to the distribution of accumulated surface energy is for one part explained by the smaller collapse time of the hemisphere and the horseshoe cavity and hence the larger maximum impact rate. In case of the hemisphere, it is again important to note that its interface evolves in exactly the same way as the interface of the isolated spherical bubble. This implies that the power focal point on the solid surface coincides with the center of a spherical bubble of the same radius, explaining why the hemisphere is most efficient in focusing its impact power on the surface. The parallel ring cavity distributes its averaged impact rate most gently on the surface. The effect of the intensity exponent n is seen from Fig. 19, which depicts the averaged impact power caused by the horseshoe cavity collapse for a variation of n. With increasing value of n, the impact power function given by Eq. (21) tends to emphasize the peak value of the local impact signal. Thus, the averaged impact power gets closer to the maximum of the impact power evolution given in Figs. 16 and 17. Furthermore, the impact distribution of the horseshoe leg exhibits an asymmetry with the focal point being shifted towards the torus center. This is explained by the horseshoe legs interacting with each other, such that the surrounding pressure field drives the collapse more efficiently from outside the torus.

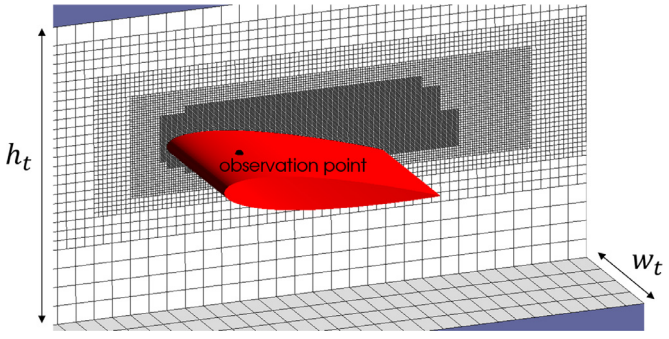

Fig. 11. Refinement levels around the NACA0015 hydrofoil for grid 1 from Table 2, where $w_t = 0.04$ m, $h_t = 2w_t$ and the foil cord length and span being 0.06 m and 0.04 m, respectively.

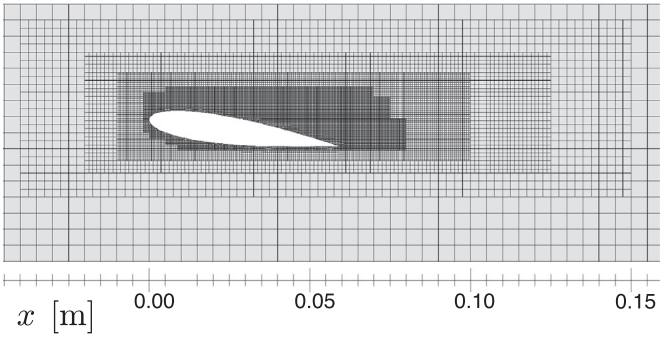

Fig. 12. Refinement levels around the NACA0015 hydrofoil for grid 1 from Table 2 (Schenke and van Terwisga, 2018).

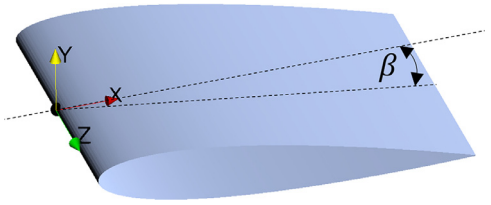

Fig. 13. Coordinate system and angle of attack $\beta = 8°$.

4.2. Cavitating flow around the NACA0015 hydrofoil

4.2.1. Convergence study

The density-pressure trajectory at the observation point in Fig. 12 (see P_0 in Table 3) is depicted in Fig. 22. The trajectory stays close to vapor pressure during phase transition and only evolves into high amplitude pressure peaks at the final stage of the condensation process. This confirms that the mass transfer coefficients are large enough to mimic realistic flow states. The grid and time

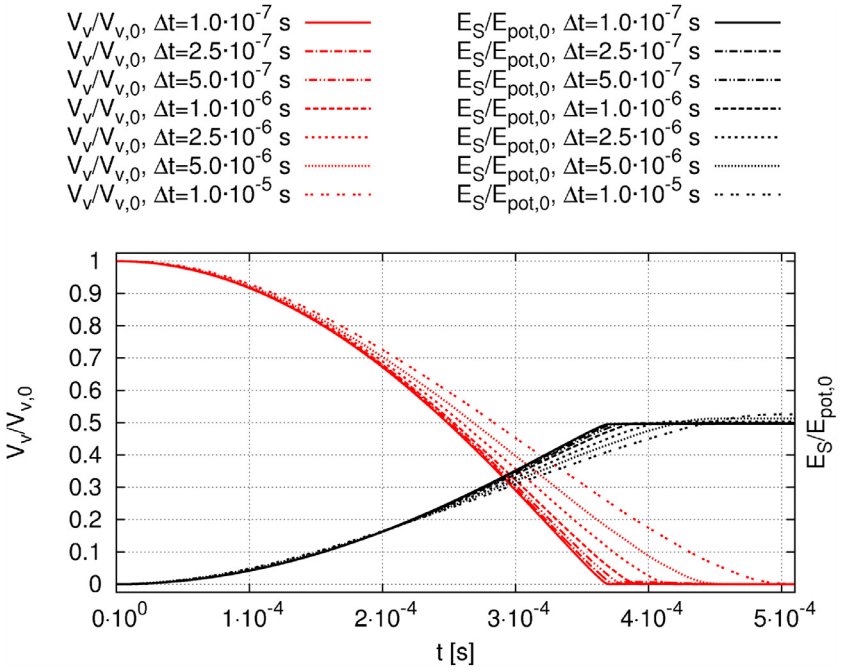

Fig. 14. Dimensionless vapor volume and surface energy accumulated over time measured from the horseshoe cavity collapse for different time step sizes, with the grid density being 55 cells/(0.02 m) (see Fig. 9).

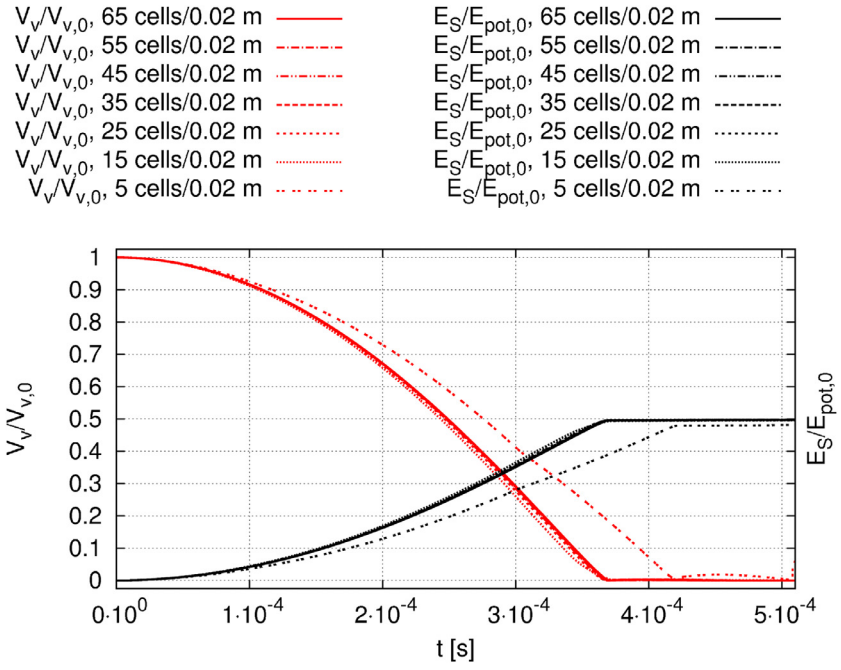

Fig. 15. Dimensionless vapor volume and surface energy accumulated over time measured from the horseshoe cavity collapse for different grid densities (see Table 1), with the time step size being $\Delta t = 10^{-7}$ s.

step sensitivity of the flow around the NACA0015 hydrofoil is assessed from the pressure fluctuations at the observation points P_1 to P_4 in Table 3, where the sample time is t^* =0.18 s. Fig. 23 shows the corresponding power spectral density distributions for $\Delta t = 7.5 \cdot 10^{-7}$ s and grid 1 from Table 2. Since the interest is on the dominating frequency only, the distributions are normalized by the peak of the corresponding first harmonic. Each distribution is smoothed by subdividing the input signal into five equidistant pieces and then calculating the mean of the so obtained Fast Fourier Transforms (FFT). In order to make the individual input signals consistent with the FFT model function, a Hanning window is applied. The low frequency harmonic obtained as an artifact of the Hanning window is not plotted. The normalized power spectral density distributions show good correlation and can be interpreted as the result of the cyclic main cavity collapses. For each investigated time step size and grid density, the mean distribution (averaged over the observation points P_1 to P_4 in Table 3 before normalization) is analyzed to identify the dominating frequency. Fig. 24 depicts the averaged power spectral density distributions for different grid densities and Δt =7.5 · 10^{-7} s. It is observed that

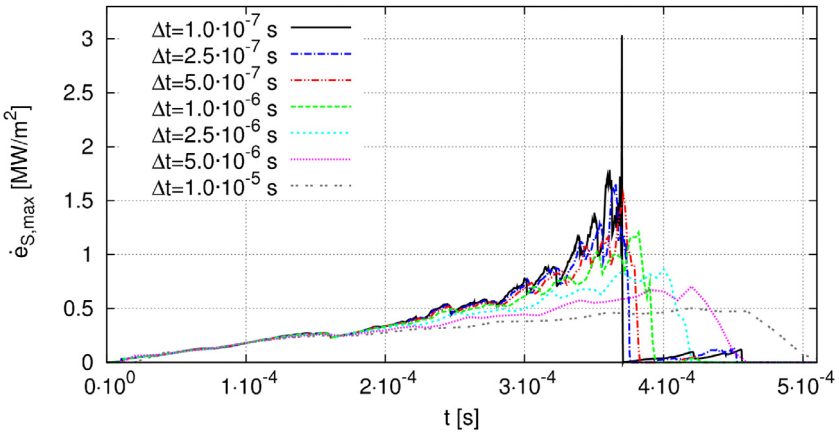

Fig. 16. Maximum surface specific impact power over time measured from the horseshoe cavity collapse for different time step sizes, with the grid density being 55 cells/(0.02 m) (see Fig. 9).

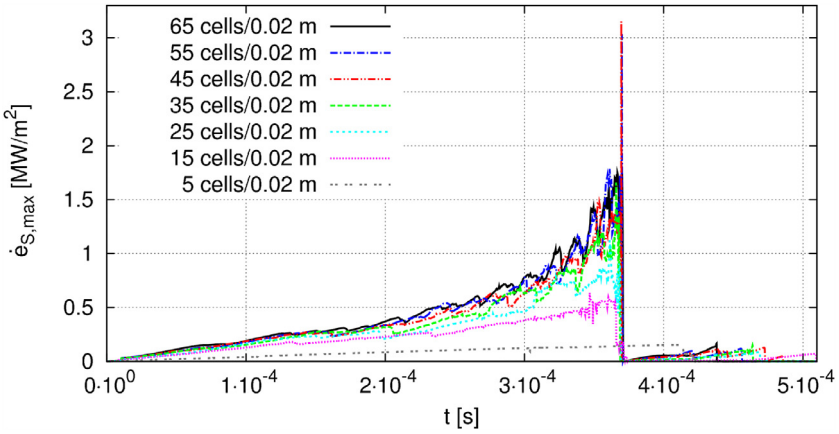

Fig. 17. Maximum surface specific impact power over time measured from the horseshoe cavity collapse for different grid densities (see Table 1), with the time step size being $\Delta t = 10^{-7}$ s.

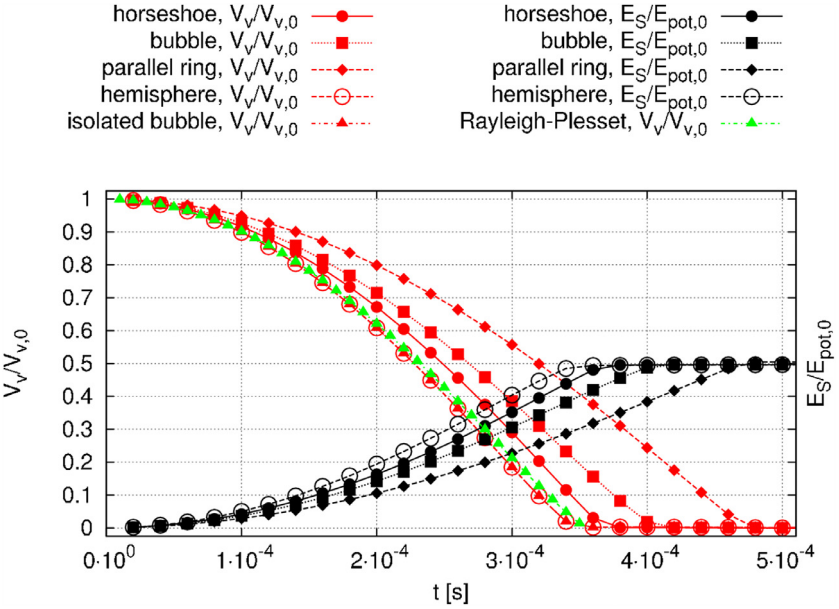

Fig. 18. Dimensionless vapor volume and accumulated surface integrated energy over time for the different cavity types depicted in Fig. 8, with the green line representing the solution obtained from the Rayleigh–Plesset equation (see Rayleigh, 1917 and Plesset, 1949). (For interpretation of the references to colour in this figure legend, the reader is referred to the web version of this article.)

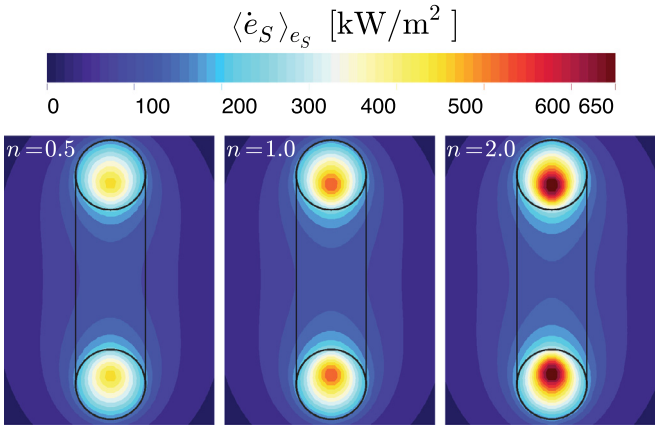

Fig. 19. Averaged surface specific impact power caused by the collapse of the horseshoe cavity depicted in Fig. 8, obtained from the impact power function $\langle \dot{e}_S \rangle_{e_S}$ given by Eq. (21) and a variation of the intensity exponent n.

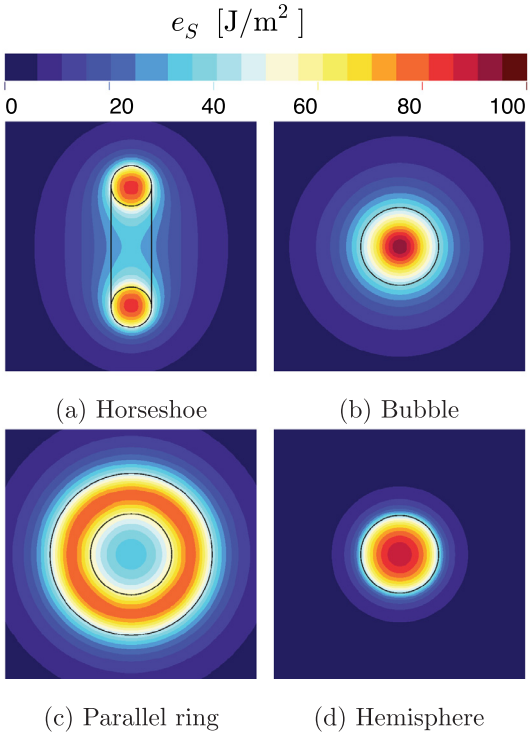

Fig. 20. Accumulated surface specific energy caused by the collapse of the cavities depicted in Fig. 8.

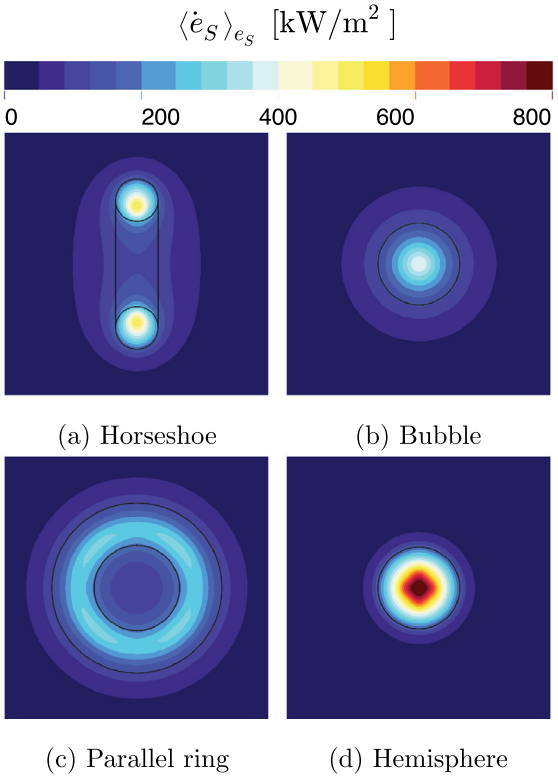

Fig. 21. Averaged surface specific impact power caused by the collapse of the cavities depicted in Fig. 8, obtained from the impact power function $\langle \dot{e}_S \rangle_{e_S}$ given by Eq. (21) and $n = 1$.

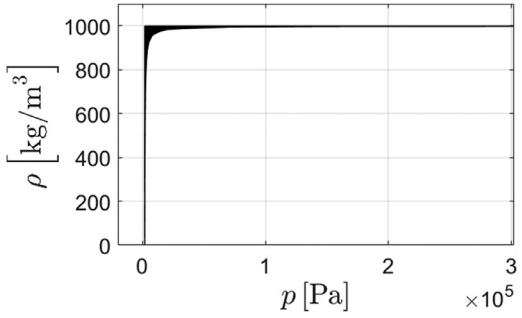

Fig. 22. $\rho - p$ trajectory on the foil surface at observation point P_0 in Table 3 (half span and 20% cord length, see Fig. 11) for $\Delta t = 7.5 \cdot 10^{-7}$ s and grid 1 from Table 2.

Table 3
Coordinates of the observation points (with respect to the coordinate system depicted in Fig. 13) for pressure and density probes.

	P_0	P_1	P_2	P_3	P_4
x [mm]	12	−100	−30	90	190
y [mm]	2.75	0	0	0	0
z [mm]	0	0	0	0	0

coarse grids tend to result in rather low frequencies of the first harmonic. The frequency of the first harmonic converges to a mesh independent value with increasing grid resolution. The same analysis is carried out for grid 1 from Table 2 and different time step sizes. For rather large time steps, the distribution in the frequency domain tends to get smeared out into the low frequency regime. The dominating frequencies are determined from a second order polynomial fit through the indicated dominating frequency and its left and right neighbor. The results for both the grid and the time step sensitivity study are summarized in Table 5. The smallest time step size $\Delta t = 7.5 \cdot 10^{-7}$ s in combination with grid 1 from Table 2 is considered to provide a physically converged solution for the further course of this study. The corresponding frequency of 192 Hz is in good agreement with the frequency of 188 Hz found by Van Rijsbergen et al. (2012) in the experiment. It is assumed that the so obtained solution of the unsteady cavitating flow field provides a reasonable estimate of the flow conditions in the experiment by Van Rijsbergen et al. (2012), even though viscosity effects such as the viscous pressure drop along the tunnel section are not present in the numerical simulation.

The convergence of the solution for the time averaged pressure field $\langle p \rangle_t$, associated with the steady driving pressure field p_d, is assessed by means of the global L_1 norm of two subsequent time steps at time instances t^j and t^{j-1}, given by

Table 4
Deviation of the accumulated surface energy measured from the horseshoe collapse simulation ($E_{S,\mathrm{simu}}$) from the theoretically exact value $E_{S,\mathrm{th}} = 1/2E_{\mathrm{pot}}(t=0)$ predicted from Eq. (18) for a flat surface stretched to infinity, with the error measure given in percent by $\epsilon = \left(E_{S,\mathrm{simu}} - E_{S,\mathrm{th}}\right)/E_{S,\mathrm{th}}$ and negative signs indicating underprediction and positive signs indicating overprediction of accumulated surface energy.

Δt			
N_{cells}/length	10^{-7} s	10^{-6} s	10^{-5} s
55/0.02 m^{-1}	−61%	−49%	+18%
35/0.02 m^{-1}	−57%	−47%	+11%
15/0.02 m^{-1}	−45%	−39%	+5%

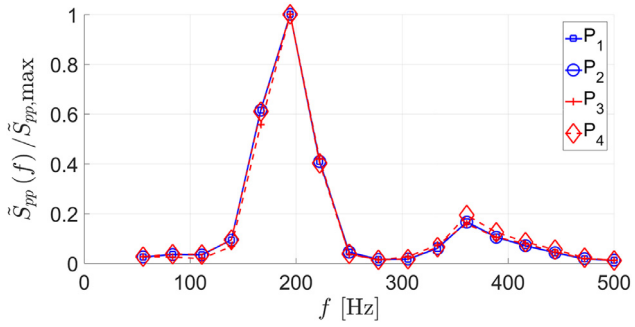

Fig. 23. Normalized power spectral density distributions of the pressure signals obtained from the observation points P_1 to P_4 in Table 3 for $\Delta t = 7.5 \cdot 10^{-7}$ s and grid 1 from Table 2.

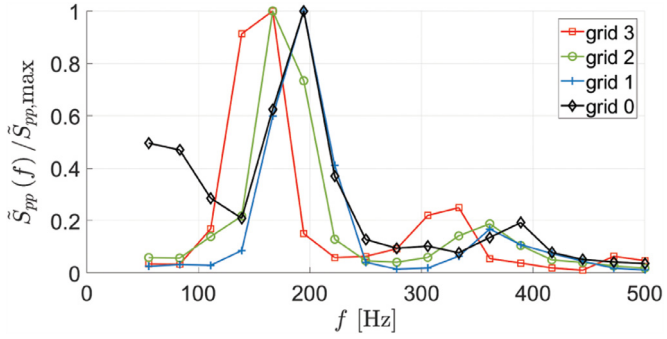

Fig. 24. Normalized distributions of the spectral power density of the pressure signals for the different grid densities in Table 2 and $\Delta t = 7.5 \cdot 10^{-7}$ s, averaged over the observation points P_1 to P_4 in Table 3 before normalization.

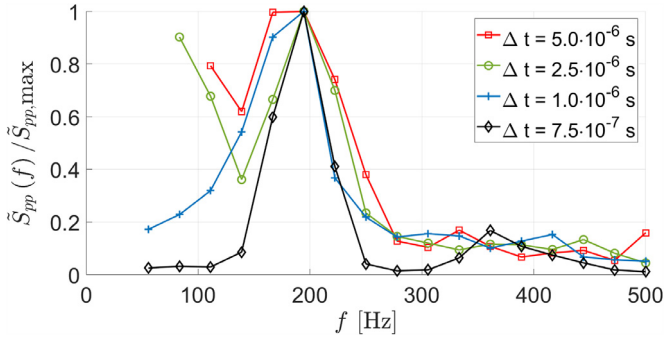

Fig. 25. Normalized distributions of the spectral power density of the pressure signals for different time step sizes and grid 1 in Table 2, averaged over the observation points P_1 to P_4 in Table 3 before normalization.

Table 5
Dominating frequencies identified from the spectra in Figs. 24 and 25 by second order polynomial interpolation of the peak values and the corresponding neighbor values. The grid sensitivity study is carried out for $\Delta t = 7.5 \cdot 10^{-7}$ s, while the time step sensitivity study is carried out for grid 1 in Table 2.

Grid no.	f [Hz]	Δt [s]	f [Hz]
0	191	$7.5 \cdot 10^{-7}$	192
1	192	10^{-6}	184
2	173	$2.5 \cdot 10^{-6}$	195
3	153	$5.0 \cdot 10^{-6}$	181

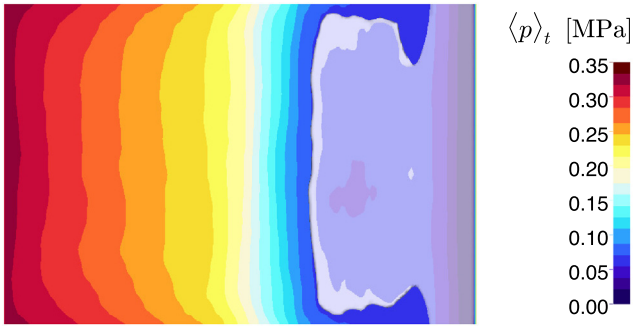

Fig. 26. Surface distribution of the time averaged pressure (see Eq. (26)) computed from cavitating flow conditions (69 shedding cycles) and a 60 kPa iso-surface of the time averaged pressure; top view with the flow from right to left.

$L_1(\langle p \rangle_t) \equiv 1/(p_\infty N_{\mathrm{cells}}) \sum_i^{N_{\mathrm{cells}}} |\langle p \rangle_{t,i}^{j} - \langle p \rangle_{t,i}^{j-1}|$. After 48 shedding cycles (0.25 s), the residual drops significantly below 10^{-5}, which is considered as a sufficiently accurate solution of the steady time averaged pressure field. In the further course of the study, the solution at 69 shedding cycles (0.36 s), is taken as a solution for the driving pressure field p_d.

4.2.2. Physical analysis of the results

The distribution of the time averaged pressure on the foil surface and a $\langle p \rangle_t$-isosurface of 60 kPa is depicted by Fig. 26. The region of maximum pressure recovery gradient is found between 40% and 50% cordlength. Cavities collapsing downstream from the pressure recovery region are associated with a significantly larger potential energy compared to cavities of the same size collapsing further upstream. The effect is clearly visible in the surface distribution of accumulated impact energy. Fig. 27 compares the accumulated surface energy e_S for the non-uniform pressure field $p_d = \langle p \rangle_t$ (right) and for a uniform driving pressure field $p_d = p_\infty = 302.3$ kPa (left). In the uniform case, energy accumulation occurs at a larger magnitude because the presence of vapor cavities lowers the average pressure in the non-uniform case. Peak pressures caused by cavity collapses tend to be filtered out by the time averaging because of the small time intervals in which they occur. The focal area in the non-uniform case is shifted further towards the trailing edge due to the pressure recovery gradient.

Fig. 28 depicts a typical sequence of a collapse event. It starts with a horseshoe cavity which developed from the break-up of a sheet cavity. With its legs attached to the surface, the horseshoe cavity collapses as it travels further downstream towards the trailing edge of the foil and thereby releases its potential energy. The instantaneous energy impact rate obtained from Eq. (13) is shown on the foil surface. It exhibits large magnitudes close to the horseshoe legs. The aggressiveness of the horseshoe cavity collapsing towards the trailing edge is enhanced by the driving pressure at the trailing edge being significantly larger than at the lead-

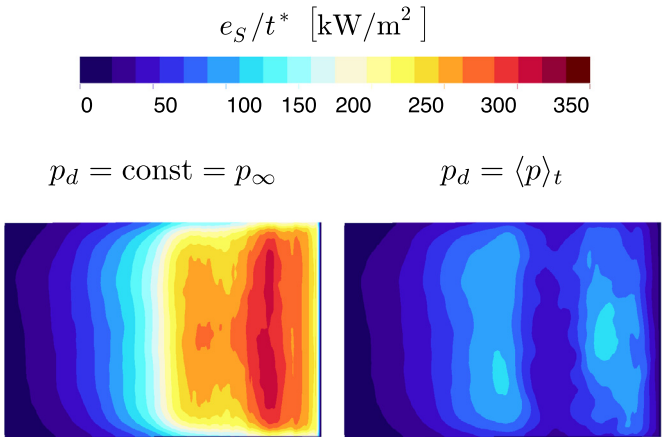

Fig. 27. Accumulated surface energy per sample time for a uniform (left) and a non-uniform (right) driving pressure field; top view on the foil surface with the flow from right to left.

ing edge. The distribution of the time averaged pressure $\langle p \rangle_t$ is depicted at the side wall. As the horsehsoe cavity collapses, another cavity is pinched off from the sheet cavity further upstream. The cavity pinch-off is induced by the re-entrant jet phenomenon, caused by the formation of a stagnation point at the sheet cavity closure. The formation of the stagnation point leads to a pronounced adverse pressure gradient driving a thin liquid jet underneath the sheet in upstream direction. When the liquid jet looses momentum, it cannot further penetrate the jet in upstream direction and is driven upward, thereby pinching of a partial cavity. The primary partial cavity may then further break up into secondary cavitating vortical structures. The rapid collapse of those secondary vortical structures is associated with a large erosive potential. A more detailed hypothesis on the underlying mechanism is found in the work by van Terwisga et al. (2009). Van Rijsbergen et al. confirm that the collapse of secondary cavitating vortical structures can lead to peak impacts (Van Rijsbergen et al., 2012). It is observed that even the primary cavities can already undergo considerable and rapid volume changes, resulting in large surface impact powers. A detailed overview on theories concerning the re-entrant jet mechanism and how this is related to the erosive aggressiveness of cavitating flows is found in the work by Dular and Petkovšek (2015). In this work, the erosive aggressiveness of the flow is assessed by means of the impact power functions given by Eqs. (21) and (22) for different values of the intensity exponent n. Fig. 29 shows corresponding impact power distributions on the foil surface for $n = 0.5$, $n = 1.0$ and $n = 2.0$, where all three distributions are depicted for the same data range of the impact power $\langle \dot{e}_S \rangle$. Fig. 30 depicts the same distributions, however normalized by the maximum values of each of the individual distributions. The simulation has been run for 0.402 s, which corresponds to 77 shedding cycles at the identified shedding frequency of 192 Hz.

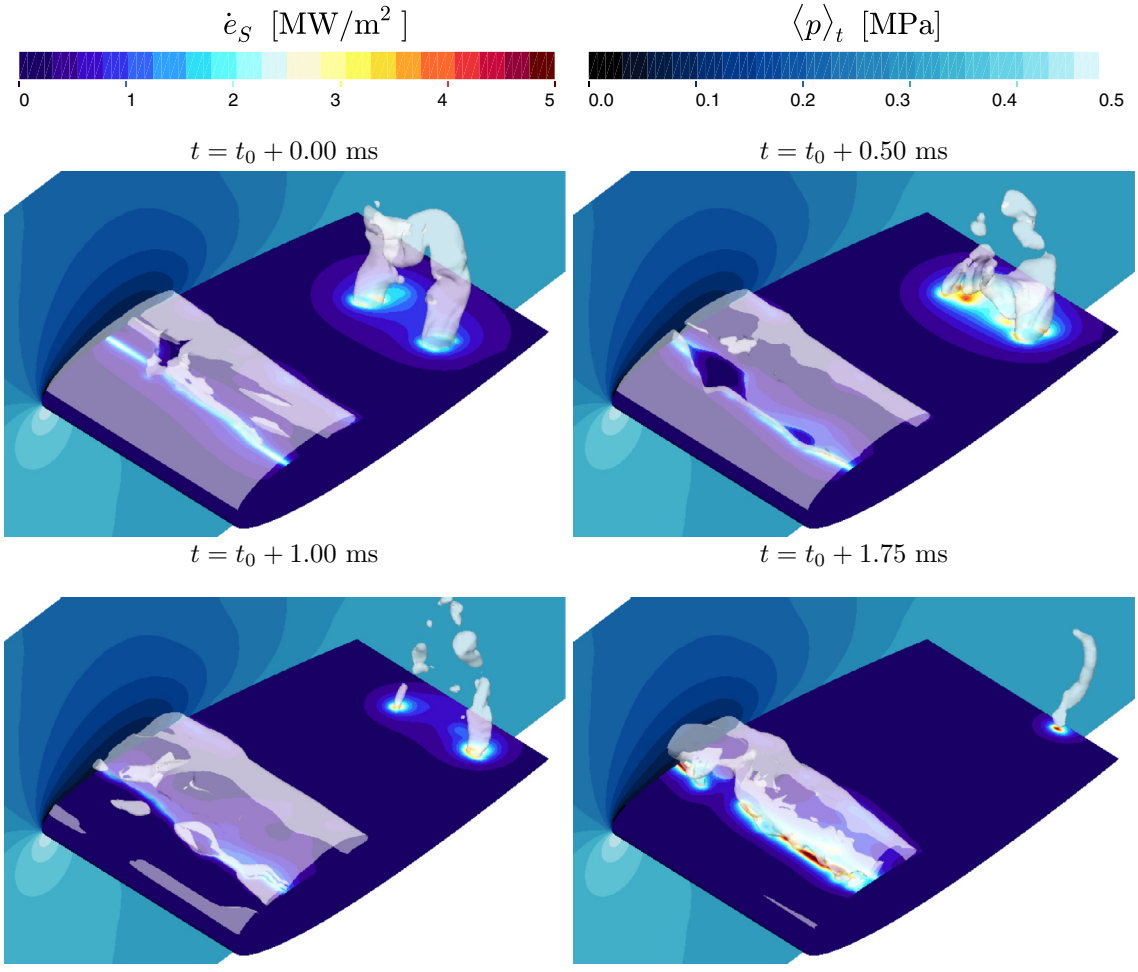

Fig. 28. Sequence of a horseshoe cavity collapse with the instantaneous impact power $\dot{e}_S$ (see Eq. (13)) depicted on the foil surface and the time averaged pressure field $\langle p \rangle_t$ (see Eq. (26)) on the tunnel side wall.

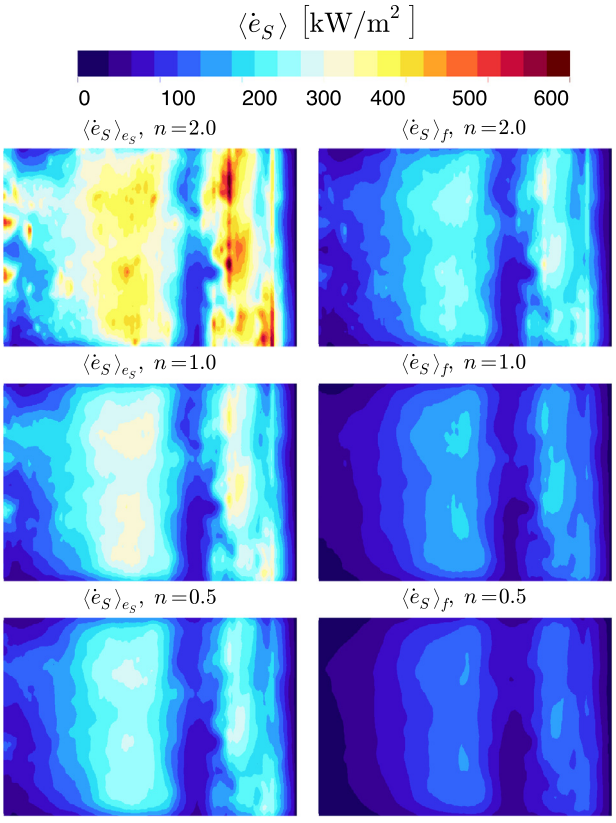

Fig. 29. Surface distributions of the averaged impact powers $\langle \dot{e}_S \rangle_{e_S}$ (left) and $\langle \dot{e}_S \rangle_f$ (right) given by Eqs. (21) and (22) for different values of the intensity exponent n; flow from right to left.

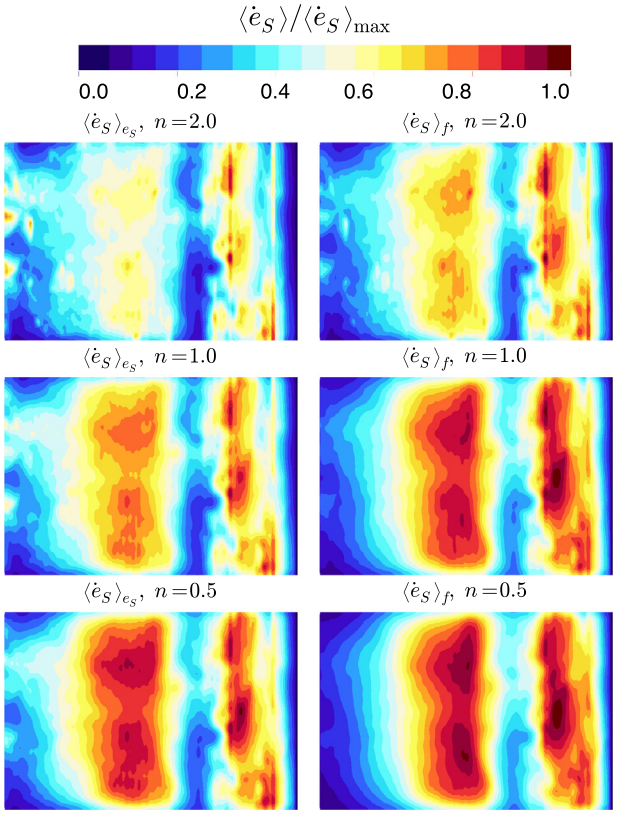

Fig. 30. Surface distributions of the averaged impact powers $\langle \dot{e}_S \rangle_{e_S}$ and $\langle \dot{e}_S \rangle_f$ depicted in Fig. 29 normalized by the maximum value of the corresponding individual distributions; flow from right to left.

Both Figs. 29 and 30 indicate two main impact areas. The first distinct impact region is located close to the leading edge at approximately 20% of the cord length from the leading edge, where cavities are typically pinched off from the sheet cavity and shed into the main flow. A large part of the shed vapor volume collapses directly downstream from the mean suction pressure peak, forming a second and rather scattered impact area. Some cavities are advected towards the trailing edge of the foil, where the impact pattern is predominantly shaped by collapsing horseshoe cavities. The dimensionless distributions in Fig. 30 show that the second impact area gets more scattered and stretches further out towards the trailing edge as n increases. This is because the collapse events at the trailing edge occur less frequently than the collapse events further upstream, but if they occur, they are more violent. For the same reason, the horseshoe footprint is also more pronounced in the surface distribution obtained from the $\langle \dot{e}_S \rangle_{e_S}$ function given by Eq. (21) than from the $\langle \dot{e}_S \rangle_f$ function given by Eq. (22), because the $\langle \dot{e}_S \rangle_f$ function value steadily decreases over times in which no significant impacts occur. The latter aspect also explains why the distribution predicted from Eq. (21) is of larger magnitude than the distribution predicted from Eq. (22), which is clearly visible from Fig. 29. It is also noted that the result obtained from the $\langle \dot{e}_S \rangle_f$ function and $n = 0.5$ exhibits strong similarity with the distribution of accumulated surface energy per time in Fig. 27 (right). The reason is that $\langle \dot{e}_S \rangle_f$ tends to the accumulated surface energy $e_S(t^*)$ per sample time t^* as the intensity exponent n tends to 0, as it has been shown from the analytical study on the impact power function response behavior. It is further observed that the intensity of the second impact area relative to the first impact area further upstream increases with increasing values of n. As shown by Fig. 32, this effect becomes even more noticeable in the $\langle \dot{e}_S \rangle_{e_S}$ distribution for $n = 4.0$, which has been obtained from a physical simulation time of 0.192 s, corresponding to 37 shedding cycles. In this case, the largest flow aggressiveness is observed close to the trailing edge, whereas the distribution obtained from $n = 1.0$ for the same simulation predicts the most aggressive events rather close to the leading edge. Again, this shows that the most violent collapse events occur close to the trailing edge, but also that those events occur less frequently such that the accumulation of energy associated with them is still smaller than for the more frequent collapse events further upstream. For both impact power functions $\langle \dot{e}_S \rangle_{e_S}$ and $\langle \dot{e}_S \rangle_f$ and all investigated values of the intensity exponent n, the transition from the first to the second impact region appears to be very sharp. Both impact regions are interrupted by a distinct low impact region.

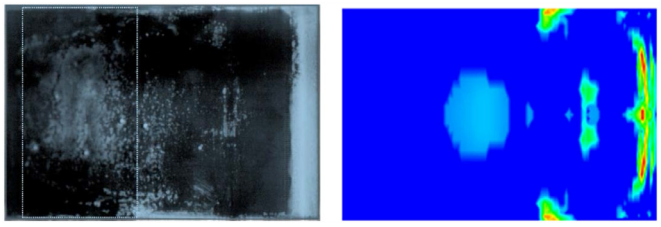

Fig. 31. Damage pattern on the NACA0015 hydrofoil surface obtained by Van Rijsbergen et al. (2012) from experimental paint tests (left) and high erosion risk areas on the same foil identified by Li et al. (2014) from numerical modeling (right, the colored figure is found in Li (2012)); results by Li et al. (2014) are obtained from the erosion risk indicator $I_{\text{Erosion}} = 1/N \sum_{i=1}^{N} I_i$, where $I_i = \partial p/\partial t$ if $\partial p/\partial t \leq$ threshold and $I_i = 0$ otherwise; flow from right to left.

As seen from Fig. 31 (left), the damage pattern obtained by Van Rijsbergen et al. (2012) from experimental paint tests show

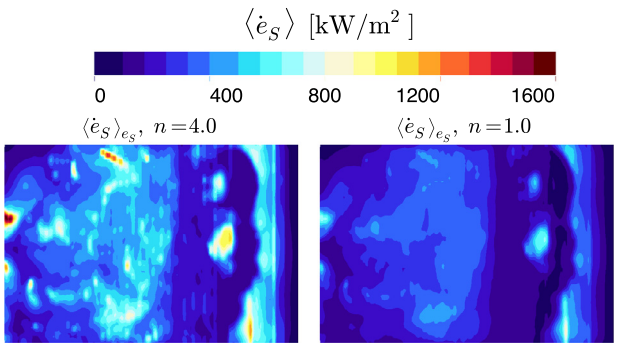

Fig. 32. Surface distribution of the averaged impact power $\langle \dot{e}_S \rangle_{e_S}$ given by Eq. (21) for $n = 4.0$ (left) and $n = 1.0$ (right), where the impact footprints resulting from the horseshoe cavity collapses at the trailing edge are more pronounced for $n = 4.0$; flow from right to left.

qualitative agreement with the numerical results. It is noted that the comparison can be of qualitative nature only. It has been shown by Mantzaris et al. (2015) that the reproducibility of paint tests is limited because the painting procedure or other parameters such as paint thickness can strongly affect the results. Distinct regions of aggressive events are identified in the cavity pinch-off region and the main cavity collapse region further downstream. Similar to the numerical results, both regions are interrupted by a region of low erosive aggressiveness. The second main impact region is observed to stretch out close to the trailing edge as well. The qualitative match of the numerically obtained impact power distribution with the experimentally obtained damage pattern increases as the intensity exponent is gradually increased from $n = 0.5$ to $n = 4.0$. The match improves in the sense that the power impact distribution in the first impact zone close to the leading edge gets less pronounced compared to the distribution in the second impact zone close to the trailing edge, and that the second impact zone stretches further towards the trailing edge as the intensity exponent n increases. Different from the approach presented in this study, Li et al. (2014) assumed the local partial pressure time derivative $\partial p/\partial t$ to be a measure for the impact aggressiveness. They derived the erosion risk indicator $I_{\text{Erosion}} = 1/N \sum_{i=1}^{N} I_i$, where $I_i = \partial p/\partial t$ if $\partial p/\partial t$ exceeds a predefined threshold level and $I_i = 0$ otherwise. As explained in Section 2.2, the approach presented in this study is based on the energy conservative conversion of potential energy into local impact power. This requires to compute the local impact from the volume change of all collapsing cavities, where the involved pressure is interpreted as the driving pressure according to the potential energy hypothesis (Vogel and Lauterborn, 1988). An impact distribution obtained by Li et al. (2014) for the same test case is depicted in Fig. 31 (right), indicating the most aggressive region right next to the leading edge. Even though the close vicinity of the leading edge had to remain unpainted in the experiment by Van Rijsbergen et al. (2012) due to the presence of roughness grains, it is likely that Li et al. (2014) overpredict the flow aggressiveness at the leading edge relative to the flow aggressiveness further downstream. The most important difference, however, is that the relative flow aggressiveness predicted from the pressure time derivative does not seem to shift towards the trailing edge when the threshold level is increased. The impacts associated with the collapse of horseshoe cavities even disappeared in the study by Li et al. (2014) when exceeding a certain threshold, whereas the leading edge impacts were still captured. This suggests that the pressure time derivative criterion fails to predict the violent cavity collapses downstream from the pressure recovery region, at least when applied in the context of unsteady RaNS equations and the mass transfer modeling approach.

5. Summary & conclusion

A new method to assess the erosive aggressiveness of cavitating flows is introduced in this study. To this end, an aggressiveness indicator is derived which is applicable to cavitating flow simulations involving mass transfer modeling as typically used for engineering problems. The indicator is derived in two steps. Starting from the potential energy hypothesis by Hammitt (1963) and Vogel and Lauterborn (1988), the first step involves an energy conservative conversion of locally radiated power into local surface impact power. A modified formulation of the cavitation intensity approach proposed by Leclercq et al. (2017) is employed in this step. Leclercq et al. (2017) have formulated a discrete energy cascade model in the sense that it involves the solid angle projection of potential energy released from the cavity collapse on triangular surface elements. In this study, a fully continuous form of the model is derived, allowing for the evaluation of the surface specific impact power on a surface point. This again facilitates the application of the model to a finite grid. The second step concerns the assessment of the aggressiveness of the cavitating flow. Two impact power functions are proposed to compute a weighted average of the local impact power. In both functions, the peak amplitudes of an impact signal are given increasing weight with increasing values of the intensity exponent n. For moderate and small values of n, the two impact power functions exhibit different behavior. The function $\langle \dot{e}_S \rangle_f$ given by Eq. (22) on the one hand returns the accumulated surface energy per sample time as $n \to 0$ and always remains active. The function given by Eq. (21) on the other hand is only active when energy intake takes place and is hence well suited to assess the aggressiveness of individual collapse events.

Grid and time step studies have been performed on idealized macroscopic cavities imploding close to a solid wall to verify the approach. The cavity collapse time has been found to be much more sensitive to time resolution than to grid resolution. Wall interaction turned out to strongly influence the rapidness of the cavity collapse. It has been shown in this study that a ring cavity parallel to a solid wall collapses much less violently than a horseshoe cavity of identical torus diameter and tube diameter. Whether a detached bubble is more aggressive than a hemispherical attached bubble of the same diameter depends on whether the focusing of accumulated energy or the focusing of impact power is taken as a measure for the flow aggressiveness. The focusing of accumulated impact energy on the one hand predicts the detached bubble to be more aggressive. The averaged impact power on the other predicts the hemisphere to be more aggressiveness. This is explained by the symmetry of the hemisphere collapse as also hypothesized by Bark et al. (2004). The collapse symmetry, however, may also partially be a result of the absence of viscous and surface tension forces in the flow simulation. A general comparison between the spherical and the toroidal shapes cannot be drawn from this study, because the flow conditions under which both cavity types typically occur in reality are very different.

The erosion risk assessment method has further been evaluated for the cavitating flow around a NACA0015 hydrofoil. A good match of the numerically obtained cavity shedding frequency with the shedding frequency identified by Van Rijsbergen et al. (2012) from the experiment is achieved. Also the break up of the shed cavities into secondary vortical cavitating structures is captured well by the inviscid flow simulation (see Schenke and van Terwigsa, 2017 and Schmidt et al., 2009). The surface impact distribution has been computed for a variation of the intensity exponent n. For $n = 0.5$, frequently impacted locations are emphasized and the obtained distribution shows strong similarity to the distribution of accumulated surface energy per sample time. For larger values up to $n = 4.0$, the impact power peaks are given more weight. This allows for the identification of locations of less frequent but high

power impacts and identifies the horseshoe cavity collapsing towards the trailing edge as a particularly violent cavity type. This finding agrees with the experimental observations by Van Rijsbergen et al. (2012). In this particular case, a good qualitative match of the impact distribution with the experimentally obtained damage pattern is achieved for rather large values of the intensity exponent n. This indicates that the removal of paint in the experiment is partially related to the aggressiveness of a few extreme situations and not purely to the accumulation of energy over time. It is concluded from both the idealized cavity collapse study and the hydrofoil test case, that it is important to know whether it is rather the accumulation of impact energy over time or the impact power magnitude of the individual collapse event that is responsible for surface erosion. Presumably, it is a combination of both, where the appropriate weight on either mechanism is hypothesized to be material dependent. The intensity exponent n proposed in this study allows us to impose a corresponding weight on the averaged impact power, where further research is needed to link the intensity exponent n to material properties. If the material is rather sensitive to the accumulation of surface energy, low values of n in the order of 1 or lower would be appropriate, whereas a strong dependency on a few isolated extreme events would be reflected by large values of n. Regardless of what the appropriate value for a specific material would be, a variation of the intensity exponent n is always helpful to clearly distinguish surface locations of high frequent but rather low power amplitude impacts from such surface locations that are impacted less frequently but at higher power amplitudes.

The largest numerical error source in the cavitation intensity approach stems from the reconstruction of the velocity divergence field, needed to compute the instantaneous release of potential energy from the individual grid cell. Compared to the uncertainty involved in the prediction of peak pressure loads from the mass transfer approach (Schenke and van Terwisga, 2017), the cavitation intensity approach still turns out to be more reliable. From the modeling point of view, the computation of the instantaneous impact power mainly suffers from two inconsistencies. One concerns the driving pressure p_d, which is typically unknown in complex flow situations. This is a problem because the driving pressure difference $p_d - p_v$ is needed to compute the potential cavity energy and hence the instantaneous power radiation from an imploding cavity. It is proposed that the driving pressure field p_d can be approximated by the steady time averaged pressure field under cavitating flow conditions, thereby providing an estimate of the ambient conditions driving the cavity collapse on statistical average (Schenke and van Terwisga, 2018). If the inflow condition is unsteady, a moving average with an appropriate time window corresponding to the time scale of the unsteady inflow might be considered. Even for cyclic flows with steady state inflow conditions, a moving time window adjusted to the characteristic period of cavity shedding might help to obtain a better estimate of the pressure field instantaneously driving the cavity collapses. The second inconsistency concerns the assumption on how the potential cavity energy is released. It is assumed that the energy release takes place instantaneously as the cavities collapse, whereas in reality the wave energy is transported by the shock wave emitted from the collapse event. It is also assumed that the energy propagates at infinite speed and not at the speed of the associated shock wave. The effect of these simplifications on the impact location is supposed to be small. This is because both the cavity collapse speed and the shock wave propagation speed can be assumed to be much larger than the advective transport in any collapse situation that is rapid enough to be potentially aggressive. However, further validation studies are needed to learn to what extent the instantaneous surface impact power obtained from the cavitation intensity approach agrees with the power signal of realistic shock waves. A more detailed comparison between signals obtained from the cavitation intensity approach and acoustic emission sensor signals (Boorsma and Fitzsimmons, 2009) obtained by Van Rijsbergen et al. (2012) for the NACA0015 hydrofoil test case investigated in this study might be of special interest.

Acknowledgments

This research is funded by the European Union Horizon 2020 Research and Innovation programme, grant agreement No. 642536, as well as by the MARIN (Maritime Research Institute Netherlands) Academy. We also highly appreciate the valuable feedback by Themistoklis Melissaris (Wärtsilä Netherlands B.V. in Drunen and TU Delft), Duncan R. van der Heul (TU Delft) and Saad Jahangir (TU Delft) on the ongoing research.

References

Arabnejad, M.H., Bensow, R., 2017. A methodology to identify erosive collapse events in the incompressible simulation of cavitating flows. In: Proceedings of the 20th Numerical Towing Tank Symposium, the Netherlands.
Bark, G., Berchiche, N., Grekula, M., 2004. Application of Principles for Observation and Analysis of Eroding Cavitation, EROCAV Observation Handbook. Department of Shipping and Marine Technology, Chalmers University of Technology, Sweden. 3.1 edition
Bhatt, M., Gnanaskandan, A., Mahesh, K., 2015. Evaluation of finite rate homogenous mixture model in cavitation bubble collapse. J. Phys. Conf. Ser. 656, 012136.
Boorsma, A., Fitzsimmons, P., 2009. Quantification of cavitation impacts with acoustic emissions techniques. In: Proceedings of the 7th International Symposium on Cavitation, Ann Arbor, Michigan, USA.
Chahine, G.L., Genoux, P.F., 1983. Collapse of a cavitating vortex ring. J. Fluids Eng. - Trans ASME - J Fluid Eng 105.
Cole, R.H., 1948. Underwater Explosions. Princeton, Princeton Univ. Press.
Dular, M., Petkovšek, M., 2015. On the mechanisms of cavitation erosion – coupling high speed videos to damage patterns. Exp. Therm Fluid Sci. 68.
Dular, M., Stoffel, B., Širok, B., 2006. Development of a cavitation erosion model. Wear 261 (5), 642–655.
Flageul, C., Patella, R.F., Archer, A., 2012. Cavitation erosion prediction by numerical cavitation. In: Proceedings of the 14th International Symposium on Transport Phenomena and Dynamics of Rotating Machinery, Honolulu, HI, USA.
Fortes Patella, R., Archer, A., Flageul, C., 2012. Numerical and experimental investigations on cavitation erosion. IOP Conference Series: Earth and Environmental Science 15, 022013.
Fortes Patella, R., Reboud, J.-L., 1998. A new approach to evaluate the cavitation erosion power. J. Fluids Eng. 120, 335–344.
Fortes Patella, R., Reboud, J.-L., Briançon-Marjollet, L., 2004. A phenomenological and numerical model for scaling the flow agressiveness in cavitation erosion. Cavitation Erosion EROCAV Workshop. Val de Reuil, France.
Frikha, S., Coutier-Delgosha, O., Astolfi, J.A., 2009. Influence of the cavitation model on the simulation of cloud cavitation on 2d foil section. Int. J. Rotating Mach. 2008.
Ghahramani, E., Bensow, R.E., 2018. Analysis of the finite mass transfer models in the numerical simulation of bubbly flows. In: Proceedings of the 10th International Symposium on Cavitation, Baltimore, Maryland, USA.
Hammitt, F.G., 1963. Observations on cavitation damage in a flowing system. J. Basic Eng. 85 (3), 347–356.
Jasak, H., 1996. Error Analysis and Estimation for the Finite Volume Method with Applications to Fluid Flows Ph.D. thesis. Imperial College.
Kato, H., Konno, A., Maeda, M., Yamaguchi, H., 1996. Possibility of quantitative prediction of cavitation erosion without model test. J. Fluids Eng. 118.
Kawanami, Y., Kato, H., Yamaguchi, H., Maeda, M., Nakasumi, S., 2002. Inner structure of cloud cavity on a foil section. JSME Int. J. Ser. B Fluids Therm. Eng. 45 (3), 655–661. doi:10.1299/jsmeb.45.655.
Koukouvinis, P., Gavaises, M., 2015. Simulation of throttle flow with two phase and single phase homogenous equilibrium model. J. Phys. Conf. Ser. 656, 012086.
Leclercq, C., Archer, A., Patella, R.F., Cerru, F., 2017. Numerical cavitation intensity on a hydrofoil for 3d homogeneous unsteady viscous flows. Int. J. Fluid Mach. Syst. 10 (3), 254–263.
van Leer, B., 1974. Towards the ultimate conservative difference scheme. ii. monotonicity and conservation combined in a second-order scheme. J. Comput. Phys. 14 (4), 361–370. doi:10.1016/0021-9991(74)90019-9.
Li, Z., 2012. Assessment of Cavitation Erosion with a Multiphase Reynolds-Averaged Navier–Stokes Method Ph.D. thesis. Technische Universiteit Delft.
Li, Z., Pourquie, M., van Terwisga, T.J.C., 2014. Assessment of cavitation erosion with a urans method. J. Fluids Eng. 136, 041101–041101–11.
Lush, P.A., 1983. Impact of a liquid mass on a perfectly plastic solid. J. Fluid Mech. 135, 373–387.
Mantzaris, A., Aktas, B., Fitzsommons, P., Atlar, M., 2015. Establishment and verification of reproducible method for coating propeller blades for erosive cavitation detection. In: 4th International Conference on Advanced Model Measurement Technologies for the Maritime Industry.

Melissaris, T., Bulten, N., van Terwisga, T.J.C., 2018. On cavitation aggressiveness and cavitation erosion on marine propellers using a urans method. In: Proceedings of the 10th International Symposium on Cavitation, Baltimore, Maryland, USA.
Merkle, C.L., Feng, J.Z., Buelow, P.E.O., 1998. Computational modeling of the dynamics of sheet cavitation. In: Proceedings of the 3rd International Symposium on Cavitation, Grenoble, France.
Mihatsch, M.S., Schmidt, S.J., Adams, N.A., 2015. Cavitation erosion prediction based on analysis of flow dynamics and impact load spectra. Phys Fluids 27.
Morgut, M., Nobile, E., 2011. Influence of the mass transfer model on the numerical prediction of the cavitating flow around a marine propeller. In: Proceedings of the 2nd International Symposium on Marine Propulsors.
Moukalled, F., Mangani, L., Darwish, M., 2015. The Finite Volume Method in Computational Fluid Dynamics: An Advanced Introduction with OpenFOAM and Matlab, 1st ed. Springer Publishing Company, Incorporated.
Nohmi, M., Ikohagi, T., Iga, Y., 2008. Numerical prediction method of cavitation erosion. In: 2008 Proceedings of the ASME Fluids Engineering Division Summer Conference, FEDSM 2008, Vol. 1.
Obreschkow, D., Tinguely, M., Dorsaz, N., Kobel, P., de Bosset, A., Farhat, M., 2011. Universal scaling law for jets of collapsing bubbles. Phys. Rev. Lett. 107, 204501.
van Oosterom, A., Strackee, J., 1983. The solid angle of a plane triangle. IEEE Trans. Biomed. Eng. 30, 125–126.
OpenFOAM, 2018. Openfoam website.
Pereira, F., Avellan, F., Dupont, P., 1998. Prediction of cavitation erosion: an energy approach. J. Fluids Eng. 120 (4), 719–727.
Plesset, M.S., 1949. The dynamics of cavitation bubbles. J. Appl. Mech. 16, 277–282.
Plesset, M.S., Chapman, R.B., 1971. Collapse of an initially spherical vapour cavity in the neighbourhood of a solid boundary. J. Fluid Mech. 47, 283–290.
Rayleigh, L., 1917. Viii. on the pressure developed in a liquid during the collapse of a spherical cavity. The London, Edinburgh, Dublin Philos . Mag. J. Sci. 34 (200), 94–98.
Van Rijsbergen, M., Foeth, E.-J., Fitzsimmons, P., Boorsma, A., 2012. High-speed video observations and acoustic-impact measurements on a naca 0015 foil. In: Proceedings of the 8th International Symposium on Cavitation, Singapore, pp. 958–964.
Schenke, S., van Terwisga, T.J.C., 2017. Simulating compressibility in cavitating flows with an incompressible mass transfer flow solver. In: Proceedings of the 5th International Symposium on Marine Propulsors, Espoo, Finland.
Schenke, S., van Terwisga, T.J.C., 2018. Erosive aggressiveness of collapsing cavitating structures. In: Proceedings of the 10th International Symposium on Cavitation, Baltimore, Maryland, USA.
Schmidt, S.J., Mihatsch, M., Thalhamer, M., Schnerr, G.H., Adams, N.A., 2011. Assessment of the prediction capability of a thermodynamic cavitation model for the collapse characteristics of a vapor-bubble cloud. WIMRC Cavitation Forum 2011, Warwick, UK.
Schmidt, S.J., Thalhamer, M., Schnerr, G.H., 2009. Inertia controlled instability and small scale structures of sheet and cloud cavitation. In: Proceedings of the 7th International Symposium on Cavitation, Ann Arbor, Michigan, USA.
Sezal, I.H., 2009. Compressible Dynamics of Cavitating 3-D Multi-Phase Flows Ph.D. thesis. Technische Universiät München.
Schenke, S., van Terwigsa, T.J.C., 2017. Numerical prediction of vortex dynamics in inviscid sheet cavitation. In: Proceedings of the 20th Numerical Towing Tank Symposium, Wageningen, the Netherlands.
van Terwisga, T.J.C., Fitzsimmons, P.A., Li, Z., Foeth, E.J., 2009. Cavitation erosion- a review of physical mechanisms and erosion risk models. In: Proceedings of the 7th International Symposium on Cavitation, Ann Arbor, Michigan, USA.
Vogel, A., Lauterborn, W., 1988. Acoustic transient generation by laser-produced cavitation bubbles near solid boundaries. J. Acoust. Soc. Am. 84, 719–731.
Warming, R.F., Beam, R.M., 1975. Upwind second-order difference schemes and applications in unsteady aerodynamic flows. In: Proceedings of the 2nd Computational Fluid Dynamics Conference, Hartford, Connecticut, USA.